Neutron-induced fission cross sections of 232Th and 233U up to 1 GeV using parallel plate avalanche counters at the CERN n_TOF facility

(n_TOF Collaboration) Tarrío, D.; Tassan-Got, L.; Duran, I.; Leong, L. S.; Paradela, C.; Audouin, L.; Leal-Cidoncha, E.; Le Naour, C.; Caamaño, M.; Ventura, A.; ...

Neutron-induced fission cross sections of ^{232}Th and ^{233}U up to 1 GeV using parallel plate avalanche counters at the CERN n_TOF facility

D. Tarrío [1,2,*] L. Tassan-Got,[3] I. Duran,[2] L. S. Leong,[3] C. Paradela,[2,4] L. Audouin,[3] E. Leal-Cidoncha,[2] C. Le Naour,[3]
M. Caamaño,[2] A. Ventura,[5] S. Altstadt,[6] J. Andrzejewski,[7] M. Barbagallo,[8] V. Bécares,[9] F. Bečvář,[10] F. Belloni,[11]
E. Berthoumieux,[11,12] J. Billowes,[13] V. Boccone,[12] D. Bosnar,[14] M. Brugger,[12] M. Calviani,[12] F. Calviño,[15] D. Cano-Ott,[9]
C. Carrapiço,[16] F. Cerutti,[12] E. Chiaveri,[12] M. Chin,[12] N. Colonna,[8] G. Cortés,[15] M. A. Cortés-Giraldo,[17] M. Diakaki,[18]
C. Domingo-Pardo,[19] N. Dzysiuk,[20] C. Eleftheriadis,[21] A. Ferrari,[12] K. Fraval,[11] S. Ganesan,[22] A. R. García,[9] G. Giubrone,[19]
M. B. Gómez-Hornillos,[15] I. F. Gonçalves,[16] E. González-Romero,[9] E. Griesmayer,[23] C. Guerrero,[12] F. Gunsing,[11]
P. Gurusamy,[22] D. G. Jenkins,[24] E. Jericha,[23] Y. Kadi,[12] F. Käppeler,[25,†] D. Karadimos,[18] P. Koehler,[26] M. Kokkoris,[18]
M. Krtička,[10] J. Kroll,[10] C. Langer,[6] C. Lederer,[6,27] H. Leeb,[23] R. Losito,[12] A. Manousos,[21] J. Marganiec,[7] T. Martínez,[9]
C. Massimi,[28] P. F. Mastinu,[20] M. Mastromarco,[8] M. Meaze,[8] E. Mendoza,[9] A. Mengoni,[29] P. M. Milazzo,[30] F. Mingrone,[28]
M. Mirea,[31,†] W. Mondalaers,[4] A. Pavlik,[27] J. Perkowski,[7] A. Plompen,[4] J. Praena,[17,32] J. M. Quesada,[17] T. Rauscher,[33]
R. Reifarth,[6] A. Riego,[15] M. S. Robles,[2] F. Roman,[12,31] C. Rubbia,[12,34] R. Sarmento,[16] P. Schillebeeckx,[4] S. Schmidt,[6]
G. Tagliente,[8] J. L. Tain,[19] A. Tsinganis,[12] S. Valenta,[10] G. Vannini,[28] V. Variale,[8] P. Vaz,[16] R. Versaci,[12] M. J. Vermeulen,[24]
V. Vlachoudis,[12] R. Vlastou,[18] A. Wallner,[27] T. Ware,[13] M. Weigand,[6] C. Weiß,[23] T. J. Wright,[13] and P. Žugec[14]

(The n_TOF Collaboration)[‡]

[1]*Department of Physics and Astronomy, Uppsala University, Box 516, 75120 Uppsala, Sweden*
[2]*Universidade de Santiago de Compostela, Spain*
[3]*Université Paris-Saclay, CNRS/IN2P3, IJCLab, 91405 Orsay, France*
[4]*European Commission, Joint Research Centre (JRC), Retieseweg 111, B-2440 Geel, Belgium*
[5]*Istituto Nazionale di Fisica Nucleare, Bologna, Bologna, Italy*
[6]*Johann-Wolfgang-Goethe Universität, Frankfurt, Germany*
[7]*Uniwersytet Łódzki, Lodz, Poland*
[8]*Istituto Nazionale di Fisica Nucleare, Bari, Italy*
[9]*Centro de Investigaciones Energeticas Medioambientales y Tecnológicas (CIEMAT), Madrid, Spain*
[10]*Charles University, Prague, Czech Republic*
[11]*Commissariat à l'Énergie Atomique (CEA) Saclay - Irfu, Gif-sur-Yvette, France*
[12]*European Organization for Nuclear Research (CERN), Geneva, Switzerland*
[13]*University of Manchester, Oxford Road, Manchester, United Kingdom*
[14]*Department of Physics, Faculty of Science, University of Zagreb, Zagreb, Croatia*
[15]*Universitat Politecnica de Catalunya, Barcelona, Spain*
[16]*Instituto Tecnológico e Nuclear, Instituto Superior Técnico, Universidade Técnica de Lisboa, Lisboa, Portugal*
[17]*Universidad de Sevilla, Seville, Spain*
[18]*National Technical University of Athens (NTUA), Athens, Greece*
[19]*Instituto de Física Corpuscular, CSIC-Universidad de Valencia, Valencia, Spain*
[20]*Istituto Nazionale di Fisica Nucleare, Laboratori Nazionali di Legnaro, Legnaro, Italy*
[21]*Aristotle University of Thessaloniki, Thessaloniki, Greece*
[22]*Bhabha Atomic Research Centre (BARC), Mumbai, India*
[23]*Atominstitut, Technische Universität Wien, Vienna, Austria*
[24]*University of York, Heslington, York, United Kingdom*
[25]*Karlsruhe Institute of Technology, Campus Nord, Institut für Kernphysik, Karlsruhe, Germany*
[26]*Oak Ridge National Laboratory (ORNL), Oak Ridge, Tennessee 37831, USA*
[27]*Faculty of Physics, University of Vienna, Vienna, Austria*
[28]*Dipartimento di Fisica, Università di Bologna, and Sezione INFN di Bologna, Bologna, Italy*
[29]*Agenzia Nazionale per le Nuove Tecnologie, l'Energia e lo Sviluppo Economico Sostenibile (ENEA), Bologna, Italy*
[30]*Istituto Nazionale di Fisica Nucleare, Trieste, Italy*
[31]*Horia Hulubei National Institute of Physics and Nuclear Engineering - IFIN HH, Bucharest-Magurele, Romania*
[32]*Universidad de Granada, Granada, Spain*

---

[*]diego.tarrio@physics.uu.se
[†]Deceased.
[‡]www.cern.ch/ntof

[33]*Department of Physics and Astronomy, University of Basel, Basel, Switzerland*
[34]*Laboratori Nazionali del Gran Sasso dell'INFN, Assergi (AQ), Italy*

The neutron-induced fission cross sections of ^{232}Th and ^{233}U were measured relative to ^{235}U in a wide neutron energy range up to 1 GeV (and from fission threshold in the case of ^{232}Th, and from 0.7 eV in case of ^{233}U), using the white-spectrum neutron source at the CERN Neutron Time-of-Flight (n_TOF) facility. Parallel plate avalanche counters (PPACs) were used, installed at the Experimental Area 1 (EAR1), which is located at 185 m from the neutron spallation target. The anisotropic emission of fission fragments were taken into account in the detection efficiency by using, in the case of ^{233}U, previous results available in EXFOR, whereas in the case of ^{232}Th these data were obtained from our measurement, using PPACs and targets tilted 45° with respect to the neutron beam direction. Finally, the obtained results are compared with past measurements and major evaluated nuclear data libraries. Calculations using the high-energy reaction models INCL++ and ABLA07 were performed and some of their parameters were modified to reproduce the experimental results. At high energies, where no other neutron data exist, our results are compared with experimental data on proton-induced fission. Moreover, the dependence of the fission cross section at 1 GeV with the fissility parameter of the target nucleus is studied by combining those (p, f) data with our (n, f) data on ^{232}Th and ^{233}U and on other isotopes studied earlier at n_TOF using the same experimental setup.

I. INTRODUCTION

Accurate data on neutron-induced fission cross sections are crucial for numerous fields in fundamental and applied nuclear physics. In particular, fission cross section data above a few MeV are required for the development of a new generation of nuclear reactors that reduces the problem of the storage of the nuclear waste. In order to reduce the amount of long-lived nuclear waste that is produced, it has been proposed to substitute the presently used U/Pu fuel cycle by a cycle based on ^{232}Th, which is the only naturally existing thorium isotope. ^{232}Th is not fissile but, after a reaction initiated by the capture of a neutron, fissile ^{233}U is formed, playing an equivalent role to ^{239}Pu in the U/Pu cycle.

In order to validate different fuel cycles and reactor concepts, their performance must be studied by means of simulations that require accurate data on the nuclear reactions involved. Evaluated nuclear data are compiled in several libraries which are maintained by different nuclear data centers, such as ENDF [1], JEFF [2], and JENDL [3]. The data available in the different libraries for the main isotopes involved in the Th/U cycle present large discrepancies. For instance, differences in the evaluated cross sections for ^{232}Th(n, f) reach up to 20% in the region between 1 and 3 MeV, and around 10% at higher neutron energies. These discrepancies are too large compared to the few percent accuracy required for fast reactors [4]. Therefore, new and more precise measurements are needed to drive newer versions of the evaluations.

From the fundamental point of view, high-resolution fission cross section data in a wide range of neutron energies are needed to deepen our understanding of the fission process. Fission cross sections are required to describe the fission barrier of actinides, which governs the competition between decay by fission and decay by emission of gammas, neutrons, or other ions [5]. This competition also influences the amount of heat released and of the remaining actinides in the

nuclear waste. Fission cross sections of most actinides are well described by using a double-humped fission barrier [6]. However, some isotopes in the vicinity of thorium (such as ^{232}Th and other nonfissile light isotopes of Th, U, and Pa) present resonances at energies around the fission threshold that cannot be explained using the same model. This behavior is called "the thorium anomaly." For such isotopes, it has been proposed to include a third potential well in their fission barrier, so that the observed resonances can be interpreted as vibrational states of a very deformed fissioning nucleus [5]. Recent theoretical studies have pointed out the need for new experimental data for all these isotopes and over a wide neutron energy range [7].

Spallation reactions induced by high-energy neutrons (≈ 100 MeV and above) can lead to fission. Neutrons with such high energies interact with individual nucleons inside the target nucleus (rather than with the nucleus as a collectivity), producing an intranuclear cascade that develops until reaching a preequilibrium state. This process is then followed by a slow decay via particle evaporation or fission. These two steps can be described by different reaction codes, such as INCL++ [8], CEM03 [9]. or ISABEL [10] for the intranuclear cascade, and ABLA07 [11] or GEMINI++ [12] for the decay. A review of the recent developments in modeling spallation-induced fission can be found in Ref. [13]. The input parameters of these codes are determined from existing experimental data, mainly from proton- and ion-induced reactions, since the neutron data in that energy region are very scarce and usually below ≈ 200 MeV. In consequence, the new experimental data at high neutron energies presented in this work provide very valuable information to benchmark and further develop the existing reaction models. They will also allow improving the quality and extending the validity range of the evaluated data libraries.

In the present work, we report on the cross sections of ^{232}Th(n, f) and ^{233}U(n, f) up to 1 GeV measured, with high

resolution, at the CERN Neutron Time-of-Flight (n_TOF) facility and using parallel plate avalanche counters (PPACs). This corresponds to the highest neutron energy available up to now and it has only been achieved previously in studies of a few other isotopes at the same facility [14–16]. These measurements are part of the extensive program carried out at the n_TOF facility to provide extended and accurate data on neutron-induced fission cross sections [17].

II. EXPERIMENTAL METHOD

The experiment was performed in two different campaigns at n_TOF. A very intense neutron flux is produced by spallation reactions on a lead target using a 20 GeV/c proton beam from the CERN Proton Synchrotron (PS). The water surrounding the spallation target acts as a moderator to produce a neutron flux covering energies from thermal up to more than 1 GeV. The 185 m long flight path between the spallation target and the experimental area (EAR1) makes high-resolution time-of-flight measurements possible. The collimator used for fission experiments (8 cm in diameter and 2.5 m long, placed 4 m before the reaction chamber) produced a beam spot of ≈ 10 cm in diameter at the experimental area, large enough to cover the whole area of the fission samples. More details on the facility and on the neutron beam spectrum can be found in Refs. [18,19]. Fission events were detected using parallel plate avalanche counters (PPACs) developed at IPN(IJCLab)-Orsay (France), which are described in Refs. [14,20], and whose main features are reported in the next section.

A. Parallel plate avalanche counters

The PPACs used in this experiment are composed of a central anode flanked by two cathodes, separated by a distance of 3.2 mm. All the electrodes are made of 1.7 μm thick and 20 × 20 cm^2 area aluminized mylar foils. The anode is connected to a voltage of around 540 V, while the cathodes are grounded. The cathodes of each PPAC are segmented in 100 strips of 1.9 mm width and with a separation of 100 μm. The strips on the pair of cathodes of each PPAC are arranged perpendicularly to each other, so that the impact point of each fission fragment can be known. Therefore, the angle formed by the segment joining the impact points of the two detected fragments and the beam axis direction can be measured for each fission event. As shown in Ref. [20], that angle is a good approximation to the emission angle of the fragments in the center-of-mass frame, so that their angular distribution can be obtained.

The fission reaction chamber contains 10 PPACs with nine samples in between, and operated with a forced flow of C_3F_8 gas at a constant pressure of 4 mbar. Fission events were identified by coincident anode signals in two adjacent PPACs, whereas the neutron energies were measured with the time-of-flight (TOF) technique: the start time was given by the signal produced by the γ-flash, created by high energy reactions at the spallation target [18], and the stop time was given by the detection of the fission fragments in the PPAC anodes.

Because the anode signals are very fast (9 ns FWHM) and PPACs electronics are quite insensitive to the γ flash, the setup is able to produce results at neutron energies as high as 1 GeV.
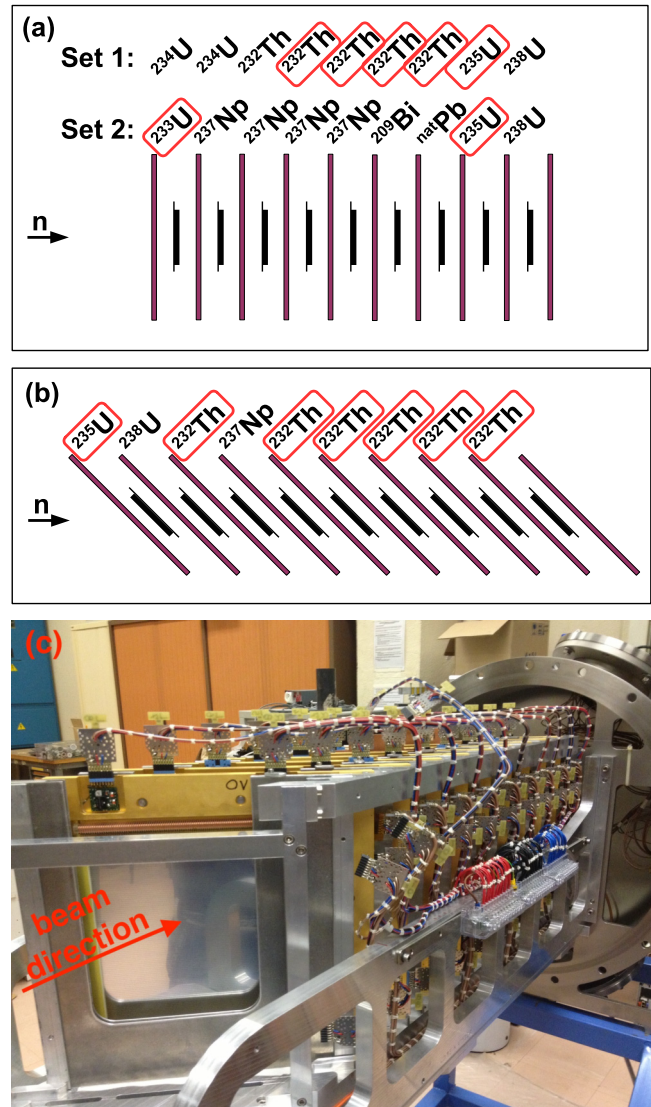

FIG. 1. Schematic views (not to scale) of the PPAC detectors and the targets used during Phase 1 (a) and Phase 2 (b). The targets studied in this work are indicated by the red rectangles. A photo of the stack of PPACs and targets used in Phase 2 can be seen in (c), where the arrow follows the neutron beam direction, and points to the aluminized electrode of the first PPAC. The active area of each PPAC is 20 × 20 cm^2.

B. Experimental configurations

The reported results are from experiments performed in two different periods and using different setups: During the Phase 1 of the n_TOF project (2001–2004), the fission cross sections of ^{233}U and ^{232}Th (together with other isotopes [14,15]) were measured using the setup shown in Fig. 1(a). Because of the limited angular acceptance of this setup, only fragments emitted at angles below about 60° with respect to the beam direction were detectable and, therefore, the complete fission fragment angular distribution (FFAD) could not be obtained.

The interest on the FFAD of ^{232}Th(n, f), due to the existence of large anisotropies, motivated another measurement

TABLE I. Masses of the ^{233}U and ^{232}Th targets used during Phase 1. The same reference sample of ^{235}U was used in Phase 1 and Phase 2.

Sample	Mass (mg)
^{232}Th (No. 1)	$11.6 \pm 3\%$
^{232}Th (No. 2)	$10.2 \pm 3\%$
^{232}Th (No. 3)	$10.3 \pm 3\%$
^{232}Th (No. 4)	$10.6 \pm 3\%$
^{233}U	$10.43 \pm 1\%$
^{235}U	$13.97 \pm 1\%$

with a new setup during Phase 2 (2010–2012). The new geometrical configuration [see Fig. 1(b)], with PPACs and targets tilted 45° with respect to the neutron beam direction, allows for a full coverage of the angular distribution of the emitted fragments [20] so that the detection efficiency can be properly taken into account, also for the data from Phase 1. In both configurations the neutron beam spot was similar, defined by the collimator previously described.

Another difference between both setups is the orientation of the actinide layer and the backing with respect to the neutron beam: In Phase 1 the backing was upstream while it was downstream in Phase 2, as schematically indicated in Figs. 1(a) and 1(b), respectively. At high neutron energies, where the linear momentum transfer to the nucleus is not negligible, the relative angle of emission between both fission fragments is no longer 180°. As a consequence, the emission angle of the fragment emitted in the backward direction increases and it must pass through a longer distance before reaching the active part of the PPAC. This induces a different variation of the efficiency beyond 30 MeV due to the momentum transfer. However, when making ratios of efficiencies in the same setup, the variation mostly cancels out and the ratio is independent of the configuration of the backing.

C. Targets

Circular samples 8 cm in diameter produced at the IPN(IJCLab)-Orsay were used in this work: one sample of ^{233}U and four samples of ^{232}Th were used in the Phase 1 measurement, while six new samples of ^{232}Th were produced for Phase 2. The same reference sample of ^{235}U was used in all measurements. A fifth sample of ^{232}Th was installed during Phase 1 but was not used in the analysis because of a problem with the data.

All the samples have a thickness between 250 and 280 μg/cm^2 and were produced by molecular plating of Th and U hydrated oxides on an aluminum foil. This foil has a thickness of 2.5 μm, except for the new ^{232}Th samples used in Phase 2, whose foils are 0.7 μm thick.

For all samples used in Phase 1, the total amount of actinide was measured by α counting in a well defined long-distance geometry (see Table I). The uncertainty includes the solid angle uncertainty, which is lower than 1%, and a statistical contribution, which is higher for the low activity samples. In addition, the nonuniformities of the deposits of the ^{235}U and ^{233}U samples were measured by α scanning by moving
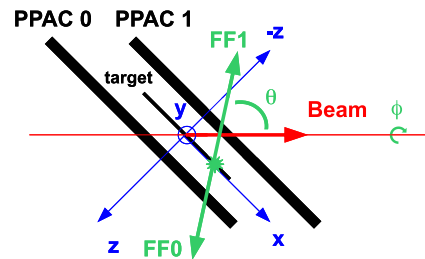

FIG. 2. Reference system used to calculate the emission angle θ of the fission fragments (FFs) in Phase 2, where PPACs and targets are tilted 45° with respect to the neutron beam direction. Fission fragments emitted at every possible value of θ between 0° and 90° can be detected. See Ref. [20] for a more detailed description.

the sample over the full area in front of a well collimated detector. In the case of the ^{232}Th samples of Phase 1, the nonuniformities were measured by Rutherford backscattering spectroscopy (RBS) by fully scanning the samples. The method was also applied to the ^{235}U reference target and agreed accurately with the α-counting method. The ^{232}Th samples of Phase 2 were not characterized in mass and uniformity. Despite their thinner backing, the electroplating was done in similar conditions and we expect thorium thicknesses similar to those used in Phase 1.

Isotopic impurities in the ^{235}U sample were measured by mass spectrometry and the ratios to the number of ^{235}U atoms resulted in ^{238}U (0.0628), ^{234}U (7.4×10^{-3}) and ^{236}U (2.7×10^{-3}). Above 1 MeV neutron energy, fissions from those isotopes were accounted for. In the other samples the contaminants are negligible.

III. DATA ANALYSIS

The data analysis is based on the detection, within a coincidence window of 10 ns, of both fission fragments in two adjacent PPACs, making it possible to reject most of the background produced by the α activity of the samples and by spallation reactions in the surrounding materials. The method, which uses the coincidence of anode signals for identifying the fission events, is described in Refs. [14,15].

The neutron energy is calculated by the TOF technique, using γ flash signals for time calibration. The γ flash mainly consists of γ rays coming from the decay of neutral pions produced when the proton beam hits the spallation target [18] and provides a common time reference within 1 ns for all the detectors. The time fluctuations on the detection of the γ flash (about 10 ns time) limit the maximum achievable neutron energy in our experiment to 1 GeV.

The emission angle of the fission fragments is obtained from the cathode signals, that provide the spatial position of each fission fragment in each PPAC. The limited angular acceptance of the setup used in Phase 1 made it impossible to get a measurement of the whole fission fragment angular angular distribution (FFAD). The situation is different in the new geometrical setup used in Phase 2 (see Fig. 2), that allows us to detect fission fragments emitted at every angle θ (although with an efficiency that depends on the angle ϕ around

the beam axis), making it possible to measure the whole FFAD (see Ref. [20] for details).

We will show (see Sec. IV B) that the detection efficiency in Phase 2 is almost insensitive to the FFAD and, therefore, it provides more accurate ratios of cross sections than Phase 1. However, since the masses of the ^{232}Th samples used during Phase 2 are unknown, we use Phase 1 to normalize the data from Phase 2.

IV. CROSS SECTION DETERMINATION

For a given neutron energy E_n, the number of detected fission events induced by neutrons in a target during the full measuring time is

$$C(E_n) = \Phi(E_n) N \sigma(E_n) \varepsilon(E_n), \tag{1}$$

where $\Phi(E_n)$ is the time-integrated neutron fluence (measured in n/(cm^2 MeV)) for the full measuring time, N is the total number of atoms in the target, $\sigma(E_n)$ is the fission cross section of the isotope, and $\varepsilon(E_n)$ is the detection efficiency. An additional correction for the counting rate from sample impurities must be included in the case of ^{235}U. Because of the thin layers composing the detection setup and the reduced beam divergence, it can be assumed that all the samples are exposed to the same neutron fluence. Therefore, the ratio of fission cross sections for two of the samples i and j is

$$\frac{\sigma_i(E_n)}{\sigma_j(E_n)} = \frac{C_i(E_n)}{C_j(E_n)} \frac{\cancel{\Phi(E_n)}}{\cancel{\Phi(E_n)}} \frac{N_j}{N_i} \frac{\varepsilon_j(E_n)}{\varepsilon_i(E_n)}. \tag{2}$$

In the resonance region (up to 10 keV), the cross section of ^{233}U was calculated using Eq. (1). In that case, the neutron fluence $\Phi(E_n)$ was deduced from the counting rate of the ^{235}U sample and the ENDF/B-VII.1 evaluation. A fit was used to eliminate the fluctuations of the fluence with the neutron energy owing to local differences between our data and the evaluation, in particular, in the valleys between resonances and at the limits of the resolved resonance region, as explained in Ref. [14].

The masses of the targets (except those of the ^{232}Th targets used in Phase 2) were accurately measured, as explained in Sec. II C. Differences in the detection efficiency for different samples will be explained in the following sections.

A. Detection efficiency

A deep analysis of the detection efficiency is a key issue for cross section measurements. The coincident detection of both fission fragments that is required to unambiguously identify the fission events affects the detection efficiency because the fragments must pass through material layers before reaching the active part of the detector. The larger the emission angle with respect to the normal to the detector, the thicker the material layers, and the lower the efficiency. Therefore, the efficiency will decrease until a high enough angle is reached. Since the value of this cutoff angle depends on the particular mass division of the fragments, a distribution of cutoff angles, caused by the mass distribution of the fragments, will be observed.

The quantity of interest in Eq. (2) is the ratio between the efficiencies of the reference and of the studied samples. Because the geometry and the materials are virtually identical for all targets in Phase 1, the ratio of detection efficiencies is expected to be nearly equal to 1 for all of them. This is not the case for Phase 2, where backings of ^{232}Th samples are much thinner than the backing of the reference sample of ^{235}U. Due to the lack of knowledge of the thickness of the ^{232}Th samples, we used Phase 1 to normalize Phase 2 data. However, even for the Phase 1 setup, there are a few deviations from unity:

$$\frac{\varepsilon_j(E_n)}{\varepsilon_i(E_n)} = 1 + \delta_{\text{thick}} + \delta_{inh} + \delta_{\text{thresh}} + \delta_{W(E_n)} \tag{3}$$

As previously discussed in Ref. [14], these deviations are due to differences in the thicknesses of the targets, backings and detectors (δ_{thick}), in the mass distribution throughout the samples (δ_{inh}), in the detection thresholds of the detectors (δ_{thresh}), and in the angular distribution $\delta_{W(E_n)}$ of fission fragments, which is different for each isotope and depends on the neutron energy. This angular distribution effect cancels out when counting rates from samples of the same isotope are compared, making it possible to estimate the magnitude of the combination of the other contributions, if several samples of the same isotope are available. In particular, δ_{inh} was assessed by folding the measured mapping of the mass distribution with the simulated beam spot relative intensity. It turns out that it is always lower than 1% because the variations of the distribution do not follow those of the neutron spot, resulting in a good average.

Figure 3 shows, for each experimental setup, the ratio between the fission yield of each ^{232}Th sample and the average. In Phase 1 the data were weighted by target masses, whereas in the case of Phase 2 data, where the masses are unknown, data were weighted by the integral of the counts in the neutron energy interval between 2.5 and 5 MeV, that will be used for normalization (see Sec. IV C). The deduced ratios are nearly energy-independent and with an average standard deviation, indicated by the horizontal lines in the figure, of $\pm 2\%$ in Phase 1 and $\pm 1.4\%$ in Phase 2, coming from δ_{thick}, δ_{inh}, and δ_{thresh}, as given in Eq. (3). These effects cannot be corrected but they are taken into account in the systematic uncertainty of the detection efficiency.

B. Anisotropy correction

The limited geometrical acceptance of the detection system requires a correction to account for the missing fragments emitted at large angles, and it depends on the angular distribution of the fragments. For each neutron energy E_n, that distribution can be described by a series of even Legendre polynomials $P_L(\cos\theta)$:

$$W(\cos\theta) = A_0 \left[1 + \sum_{L=2,\, L\text{ even}}^{L_{\max}} A_L P_L(\cos\theta) \right]. \tag{4}$$

The so-called anisotropy parameter, A, is defined as the ratio of the number of fission fragments emitted along the direction of the neutron beam with respect to the number of
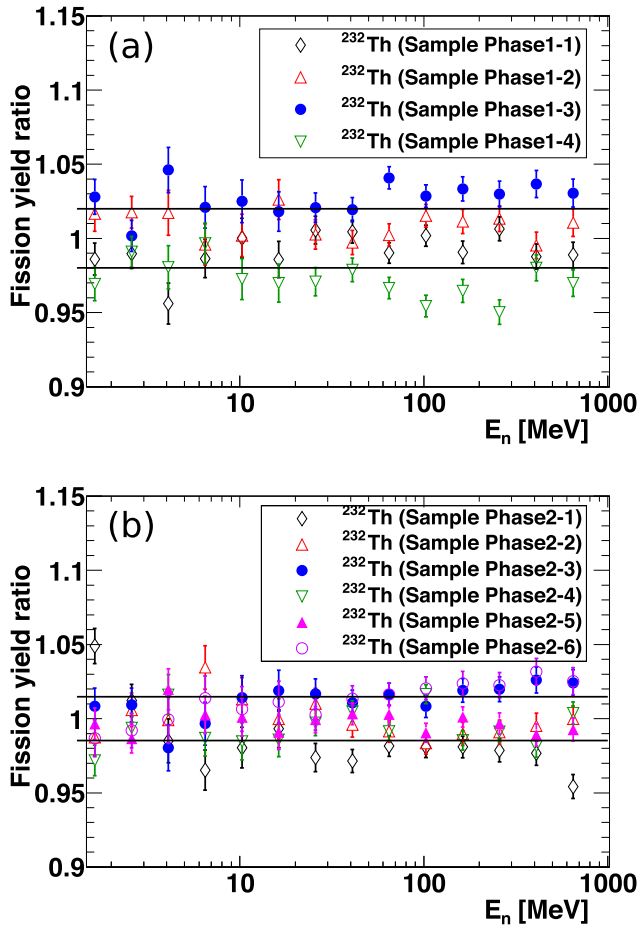
FIG. 3. Fission yield ratios between each sample of ^{232}Th and the average, during Phase 1 (a) and Phase 2 (b). The horizontal lines represent the average standard deviations.

those emitted in the perpendicular direction, as:

$$A = \frac{W(0°)}{W(90°)} = \frac{1 + A_2 + A_4 + \cdots}{1 - \frac{1}{2}A_2 + \frac{3}{8}A_4 - \cdots}. \quad (5)$$

This parameter is commonly used to give a simplified description of the angular distribution as a function of the neutron energy, by providing information only on its relative value at 0° and at 90°, while ignoring the behavior at intermediate angles. If the angular distribution is described by a Legendre polynomial expansion limited to second order, the anisotropy parameter A is directly related to the second-order coefficient A_2. Although such an approximation is usually enough, higher order fitting coefficients might be needed for a correct description of the angular distribution in certain cases. In those situations, the anisotropy parameter A is not enough to describe the full angular distribution.

Because the PPACs are position sensitive, the emission angle of the fission fragments can be determined from the trajectory reconstruction. But with the experimental setup used in Phase 1, only emission angles below $\theta \approx 60°$ are detected, which is insufficient to fit the whole angular distribution $W(\cos\theta)$. In consequence, only a barely qualitative dependence of the anisotropy parameter with the neutron
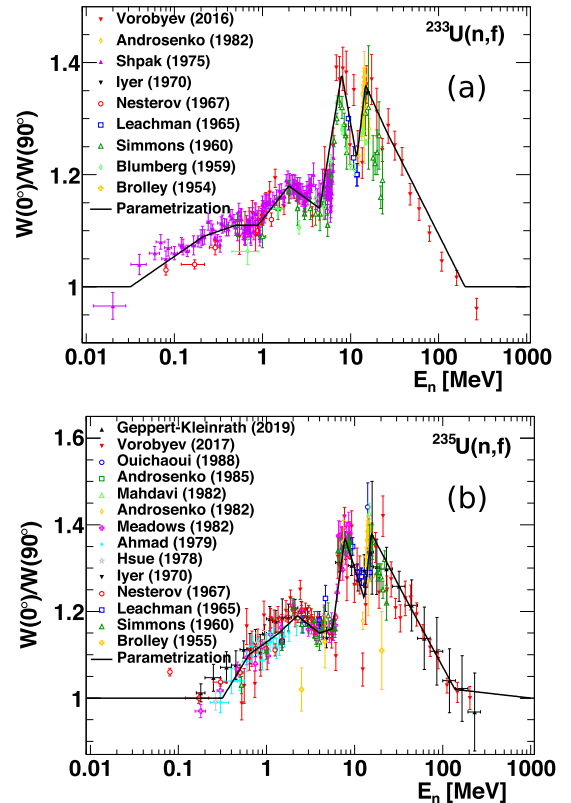

FIG. 4. Experimental values of the anisotropy parameter $A = W(0°)/W(90°)$ for the neutron-induced fission of ^{233}U (a) [23–31] and ^{235}U (b) [24,26–29,32–40] retrieved from EXFOR, as a function of the neutron energy. The solid lines represent the parametrizations of the anisotropy used in this work.

energy can be obtained, which is not enough for the present purpose of correcting for the angular acceptance of the cross-section measurement [21]. On the contrary, and thanks to the broad angular range of the setup from Phase 2, the whole angular distribution of the fragments can be measured using that new setup. That was the case for ^{232}Th, as it will be discussed further below; unfortunately, it was not possible to get the angular distribution for ^{235}U in that measurement because of the failure of one of the segmented cathodes in one of the PPACs.

Therefore, for ^{233}U (which was only measured using the Phase 1 setup) and for the reference isotope, ^{235}U, we have used the values of the anisotropy parameter A available in the EXFOR database [22] to deduce the angular distributions $W(\cos\theta)$ up to second order, for each neutron energy, using Eqs. (4) and (5). In order to cover for all the neutron energies, we have used a simple fit to the available data as it can be seen in Fig. 4. Above 200 MeV, where no data exist, the anisotropy was assumed to approach unity at 1 GeV.

On the other hand, neutron-induced fission of ^{232}Th presents much larger anisotropies than ^{233}U and ^{235}U. Moreover, it has been shown that, for certain energy intervals such as around the fission threshold, its angular distribution cannot be fully described by using only one parameter and second- and fourth-order Legendre polynomials must be included in
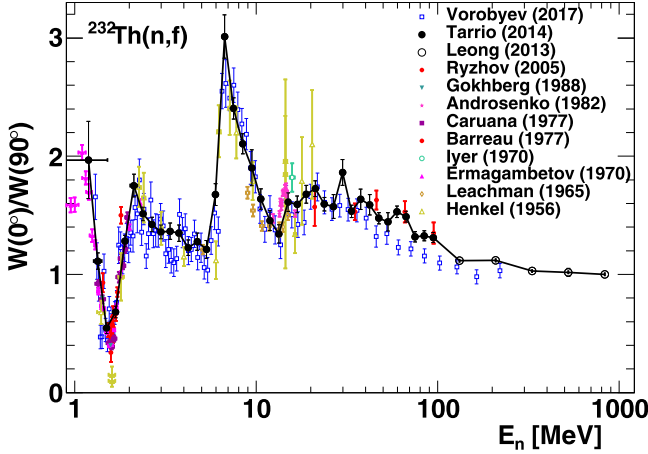
FIG. 5. Experimental values of the anisotropy parameter $A = W(0°)/W(90°)$ for the neutron-induced fission of ^{232}Th as a function of neutron energy. The solid line connects the values deduced from the experimental angular distributions measured in our earlier works [20,41], and whose fits to Eq. (4) are used in the present work. Below 100 MeV, second- and fourth-order terms were needed to describe the features of the angular distribution [20], whereas above 100 MeV, the second-order term was enough [41]. Other experimental values on the anisotropy parameter, directly retrieved from EXFOR, are shown for comparison [24,26,28,33,42–47].

the fit to Eq. (4) (see Ref. [20] for a detailed discussion). Therefore, we use the full angular distributions obtained from the present measurement of ^{232}Th from Phase 2 (tilted setup), for each neutron energy: In a first analysis, only energies below 100 MeV were considered, and the angular distributions were fitted to an expansion of Legendre polynomials up to fourth order [48]. A later analysis extended the results to 1 GeV [41] using a fit including only the second-order polynomial. The values of the anisotropy parameter A deduced from those fits, for each neutron energy, are shown in Fig. 5, and connected by solid lines for better clarity. Other experimental values of the anisotropy parameter, directly retrieved from EXFOR, are also shown for comparison [24,26,28,33,42–47].

The reduction in the geometrical efficiency for each sample i, because of the limited angular acceptance in the polar and azimuthal angles θ and ϕ, can be estimated by

$$\epsilon_i(E_n) = \frac{\int_{\phi_{\min}}^{\phi_{\max}} \int_{(\cos\theta)_{\min}}^{(\cos\theta)_{\max}} W(E_n, \cos\theta)d(\cos\theta)d\phi}{\int_{-\pi}^{+\pi} \int_0^1 W(E_n, \cos\theta)d(\cos\theta)d\phi}. \quad (6)$$

The limits in the acceptance angles θ and ϕ are determined by the geometry of the setup and by the thickness of the targets and the backings (see Table II). While in Phase 2, all the possible values from θ are accepted, in Phase 1 $\cos\theta$ is limited to 0.55, according to the GEANT4 simulations performed [20]. On the other hand, the azimuthal angle ϕ ranges from $-\pi$ to $+\pi$ radians in Phase 1, while in Phase 2, and because of the tilted geometry, the limits in ϕ are not constant but functions of θ. These functions $f_1(\cos\theta)$ and $f_2(\cos\theta)$, which depend on the target and backing thicknesses, are shown in Fig. 6 as the red contour lines derived from the GEANT4 simulations.

TABLE II. Limits in the integration angles for each setup. $\phi_{\min}$ and $\phi_{\max}$ are functions of $\cos\theta$ in Phase 2, shown as the contours in Fig. 6.

	Phase 1	Phase 2
$(\cos\theta)_{\min}$	0.55	0
$(\cos\theta)_{\max}$	1	1
$\phi_{\min}$ (rad)	$-\pi$	$f_1(\cos\theta)$
$\phi_{\max}$ (rad)	$+\pi$	$f_2(\cos\theta)$

The efficiency ratios $\epsilon(^{235}\text{U})/\epsilon(^{232}\text{Th})$ and $\epsilon(^{235}\text{U})/\epsilon(^{233}\text{U})$ can be calculated by introducing these integration limits in Eq. (6), as well as the corresponding angular distributions, leading to the results shown in Fig. 7. In the case of Phase 1, where all the targets had the same backings, the ratio of efficiencies $\epsilon(^{235}\text{U})/\epsilon(^{233}\text{U})$ (black line in the figure) is close to 1 in the whole energy range because of the similar angular behavior exhibited by both isotopes, whereas the large anisotropies of ^{232}Th lead to stronger variations with the neutron energy in the $\epsilon(^{235}\text{U})/\epsilon(^{232}\text{Th})$ ratio (red triangles). In Phase 2, the larger angular acceptance of the tilted setup makes the ratio $\epsilon(^{235}\text{U})/\epsilon(^{232}\text{Th})$ (blue squares) less sensitive to the variations in the angular distribution: at the second-chance fission threshold (≈ 7 MeV), the large anisotropy of ^{232}Th leads to a local variation in the efficiency ratio of 5% when using the tilted setup (Phase 2), compared to the 15% difference observed in the perpendicular setup (Phase 1). Moreover, in Phase 2, the ^{232}Th samples had a thinner backing than the ^{235}U sample, which explains the overall shift of the ratio $\epsilon(^{235}\text{U})/\epsilon(^{232}\text{Th})$ to lower values in comparison to the same ratio in Phase 1.

C. Normalization

As already mentioned, among all the ^{232}Th targets used in this experiment, only the masses of those used in Phase 1 were measured. Therefore, the ratio $\sigma_f(^{232}\text{Th})/\sigma_f(^{235}\text{U})$
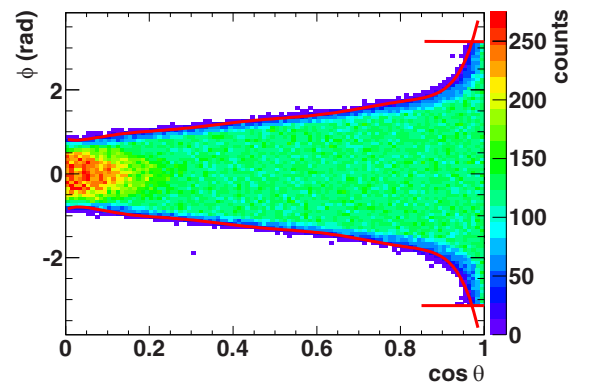

FIG. 6. Detection efficiency of the tilted setup (Phase 2) as a function of the emission angles θ and ϕ, according to GEANT4 simulations. The red lines represent the contour used to calculate the total efficiency. More details about the detection efficiency on this setup can be found in Ref. [20].
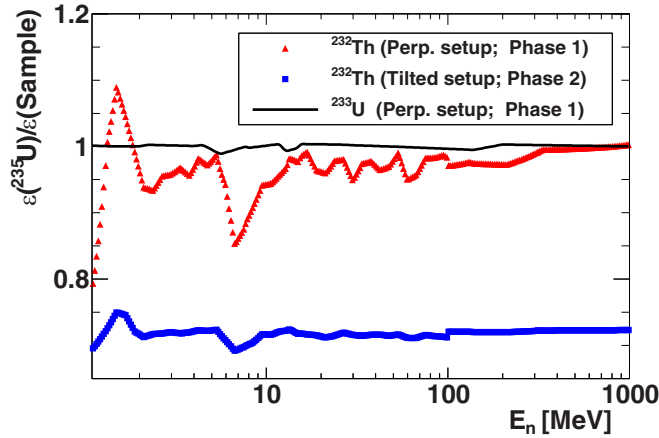
FIG. 7. Angular contribution to the detection efficiency ratios between the reference isotope ^{235}U, and the studied samples of ^{232}Th and ^{233}U.

obtained with the Phase 2 data was normalized to the same ratio obtained from Phase 1, for which the masses are well known. Given that the efficiency correction to Phase 1 data presents larger variations with the neutron energy than those from Phase 2 data and, therefore, larger systematic uncertainties, ^{232}Th data from Phase 1 were only used for normalization of the data from Phase 2. The normalization was done using the neutron energy region between 2.5 and 5 MeV, where both the fission cross section and the anisotropy of ^{232}Th are rather constant.

In the case of ^{233}U, the mass is known so that no normalization procedure was applied.

V. SYSTEMATIC UNCERTAINTIES

The systematic uncertainties in the cross section ratios are given by the uncertainties associated with the different terms in Eq. (2).

As previously mentioned, the Phase 2 ratio $\sigma_f(^{232}\text{Th})/\sigma_f(^{235}\text{U})$ is normalized to the results from Phase 1, by integrating that ratio in the energy interval from 2.5 to 5 MeV, where the correction by the angular efficiency is rather constant. Therefore, the uncertainty in the final results of the ratio $\sigma_f(^{232}\text{Th})/\sigma_f(^{235}\text{U})$ must also take into account the uncertainty from the normalization factor.

The uncertainties in the individual sample masses (see Table I) contribute to the cross section ratios with the uncertainties given in Tables III and IV. For the ratio $\sigma_f(^{232}\text{Th})/\sigma_f(^{235}\text{U})$ in Phase 1, the average of all the available targets was considered.

The largest contribution to the systematic uncertainty comes from the ratio between the efficiencies of the reference and of the studied samples, given by Eq. (3). As discussed in Sec. IV A, the sum of terms $(\delta_{\text{thick}} + \delta_{inh} + \delta_{\text{thresh}})$ gives 2% and 1.4% for the samples of ^{232}Th in Phase 1 and Phase 2, respectively. It is reasonable to expect a similar uncertainty for the ^{233}U and ^{235}U targets. Therefore, that contribution to the

TABLE III. Systematic uncertainties obtained for the present data on the ratio $\sigma_f(^{232}\text{Th})/\sigma_f(^{235}\text{U})$. See text for details.

	Uncertainty (%)	
Contribution	Normalization factor	Phase 2 final results
Sample masses ratio	1.5	–
$\delta_{\text{thick}} + \delta_{inh} + \delta_{\text{thresh}}$	2.4	2.0
$\delta_{W(E_n)}$	0.2	0.25
Normalization	–	2.8
Total	2.8	3.5

systematic uncertainty of the ratio $\sigma_f(^{232}\text{Th})/\sigma_f(^{235}\text{U})$ will be of 2% for Phase 2, and of 2.4% for the normalization region in Phase 1. In the case of $\sigma_f(^{233}\text{U})/\sigma_f(^{235}\text{U})$, that contribution amounts to 2.8%.

The uncertainty in the correction of the efficiency due to angular distribution $\delta_{W(E_n)}$ is energy dependent, and the largest contribution to the ^{232}Th case happens around the fission threshold energy, as seen in Fig. 7. Assuming a conservative 5% uncertainty in the values of the anisotropy parameters, the contribution to the uncertainty in the fission cross section ratio amounts to 0.25% for data from Phase 2; for comparison, that contribution is 0.9% for the Phase 1. The difference arises from the fact that the tilted setup used in Phase 2 is less sensitive to variations in the angular distribution because of the broader angular range covered. In any case, for ^{232}Th in Phase 1 we are only interested in the energy interval used for the normalization, where that term amounts to 0.2%. In the case of ^{233}U, the angular behavior is very similar to the one of the reference nucleus ^{235}U, and the uncertainty contribution amounts to 1%.

By summing quadratically all the contributions, the uncertainty in the normalization interval for the ratio $\sigma_f(^{232}\text{Th})/\sigma_f(^{235}\text{U})$ amounts to 2.8%, as shown in the middle column in Table III. The total systematic uncertainty for the final ratio, after the normalization, is 3.5% (right column in Table III).

In the case of the ratio $\sigma_f(^{233}\text{U})/\sigma_f(^{235}\text{U})$, the total systematic uncertainty amounts to 3.3% (see Table IV).

When converting the cross-section ratios into final cross-sections, the uncertainty of the reference cross-section used must be added.

TABLE IV. Systematic uncertainties obtained for the present data on the ratio $\sigma_f(^{233}\text{U})/\sigma_f(^{235}\text{U})$. See text for details.

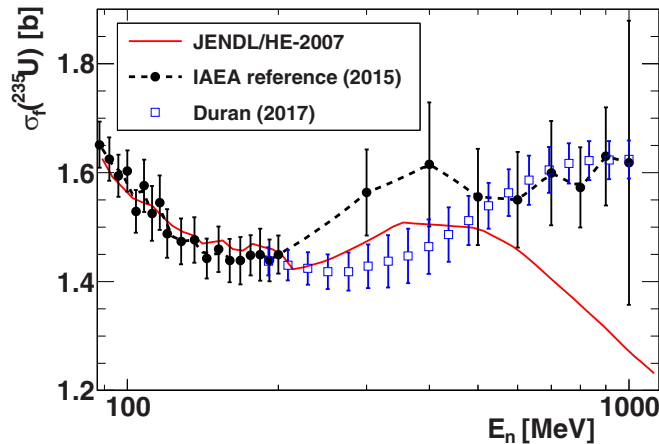| Contribution	Uncertainty (%)
Sample masses ratio	1.4
$\delta_{\text{thick}} + \delta_{inh} + \delta_{\text{thresh}}$	2.8
$\delta_{W(E_n)}$	1.0
Total	3.3

FIG. 8. Comparison of different evaluations of the ^{235}U(n, f) cross section above 100 MeV: JENDL/HE-2007 [50], the IAEA High-Energy reference [52], and the evaluation by Duran *et al.* [53].

VI. EXPERIMENTAL RESULTS

In this work, the cross section ratios for neutron-induced fission of ^{232}Th and ^{233}U, with respect to ^{235}U, were determined in a wide and continuous energy region either from fission threshold (in the case of ^{232}Th) or from 0.7 eV (in the case of ^{233}U), and up to 1 GeV in both cases.

To produce final values for the fission cross sections, the ratios must be multiplied by the reference cross section of ^{235}U(n, f), as follows from Eq. (2). The chosen reference is the IAEA standard 2017 that, above the resonance region, is a standard from 0.15 MeV up to 200 MeV [49], and complemented by the ENDF/B-VII.1 evaluation in the region between 10 and 150 keV. Due to the lack of accurate enough experimental data, the ^{235}U(n, f) is not a standard cross section above 200 MeV. Nonetheless, different evaluations are available for ^{235}U(n, f), although with important discrepancies among them. The Japanese Evaluated Nuclear Data Library High Energy File (JENDL/HE-2007) [50] provides values up to 3 GeV, and we have used it in our previous publications to obtain high-energy values of fission cross sections [14,15]. However, the behavior of this evaluation above ≈ 500 MeV has been questioned by Lo Meo *et al.* [51].

On the other hand, the IAEA has published a so-called reference cross section of ^{235}U(n, f) up to 2 GeV, based on experimental data and theoretical calculations [52]. These results are in clear disagreement with the JENDL/HE-2007 evaluation, as can be seen in Fig. 8. The same figure also shows the more recent proposal by Duran *et al.* [53], that is an update of the work from Ref. [51], and uses Monte Carlo reaction codes combined with experimental data.

In this work, we have chosen to use the evaluation by Duran *et al.* [53] to deduce the final values of the fission cross sections $\sigma_f(^{232}$Th$)$ and $\sigma_f(^{233}$U$)$ above 200 MeV. In any case, and in order to facilitate the use of our results when newer reference cross sections will become available, the ratios of the fission cross sections $\sigma_f(^{232}$Th$)/\sigma_f(^{235}$U$)$ and $\sigma_f(^{233}$U$)/\sigma_f(^{235}$U$)$ are also provided. These results do not
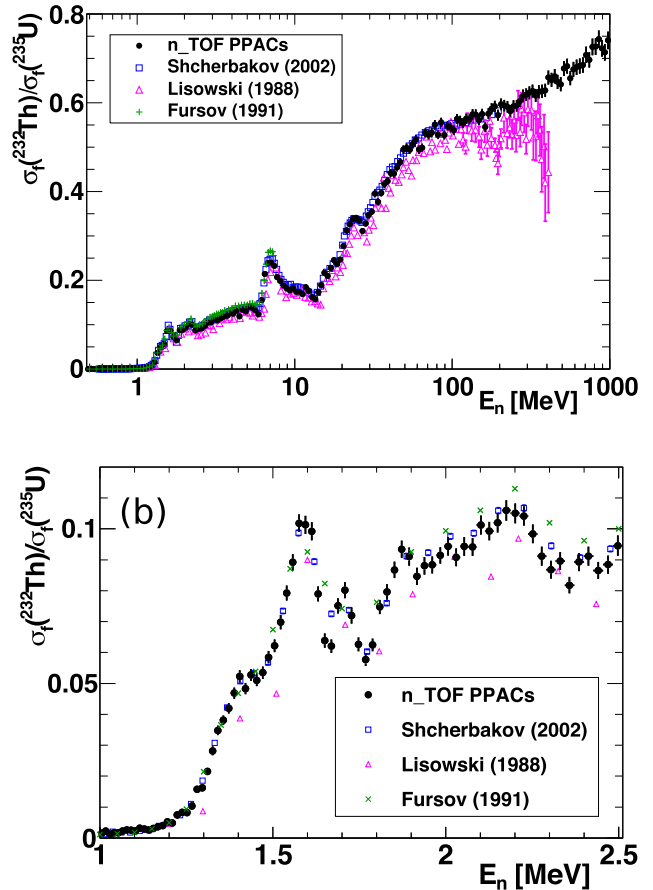
FIG. 9. Fission cross section ratio of ^{232}Th relative to ^{235}U, compared with previous results [54–56]. Panel (b) shows a detailed view around fission threshold of the full range in (a). The error bars in our data represent statistical uncertainties.

depend on evaluations and can, therefore, be considered as absolute results.

A. ^{232}Th(n, f)

The final ratio $\sigma_f(^{232}$Th$)/\sigma_f(^{235}$U$)$ is shown in Fig. 9, compared with previous results available in the EXFOR database [22]. The error bars in our data represent statistical uncertainties only. Our results are the only ones covering a broad energy range from fission threshold up to 1 GeV neutron energy. They are in good agreement with the values from Shcherbakov *et al.* [54], who measured up to 200 MeV. There is also a good agreement with the shape of the data from Lisowski *et al.* [56] up to 100 MeV, although their data are around 10% below our results; above 100 MeV, their data show very large uncertainties and the trend deviates from our values. Other authors [55,61,62] provide data in smaller energy ranges showing, in general, a good agreement with our results.

The results for $\sigma_f(^{232}$Th$)$, covering from fission threshold up to 1 GeV, are shown in Fig. 10(a), together with previous results [54,56–60] and with the ENDF/B-VIII.0 evaluation [1]. The error bars in our data represent statistical uncertainties.
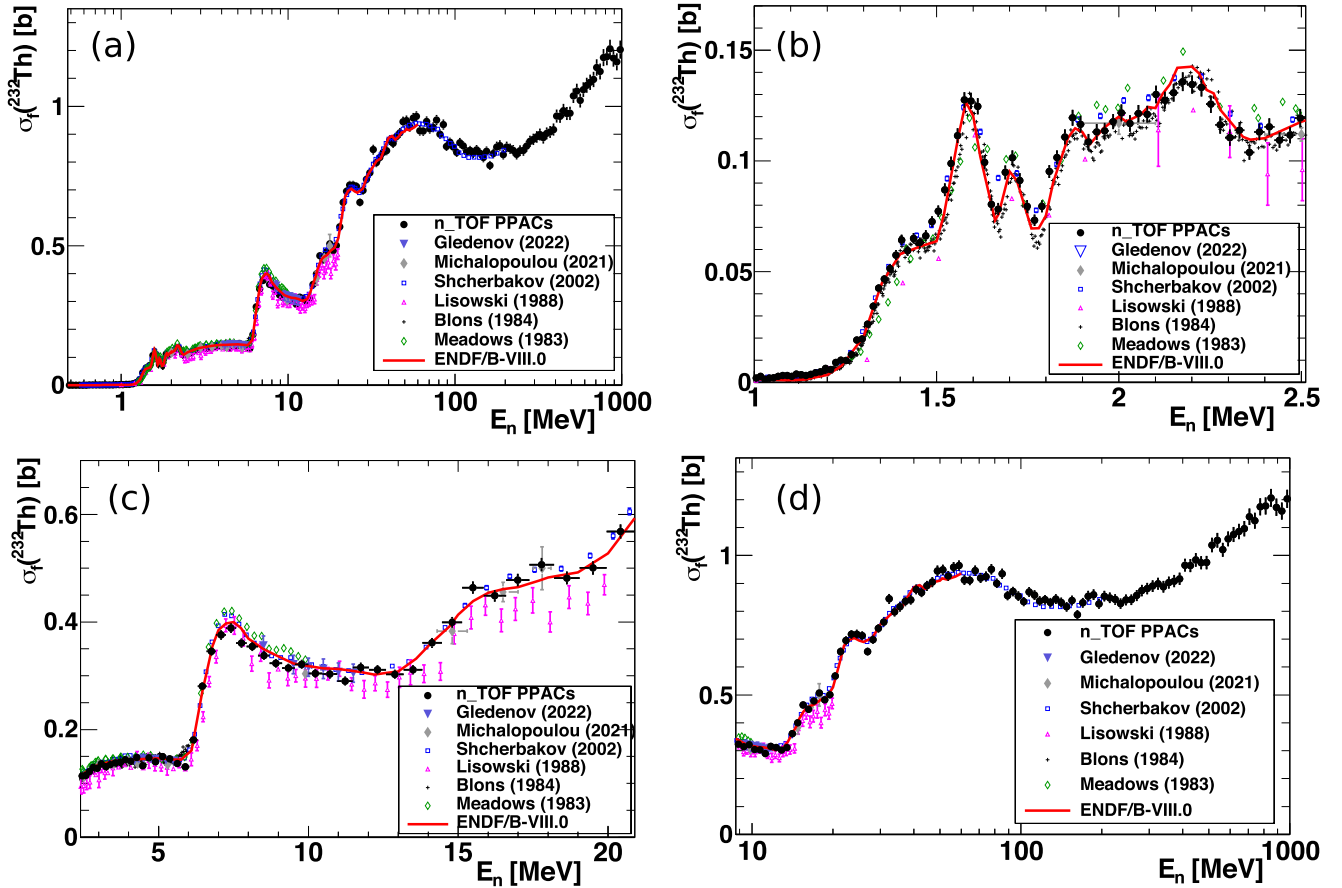
FIG. 10. The final cross section of ^{232}Th(n, f) obtained in the present work is compared with previous results available in the EXFOR database [54,56–60] and with the ENDF/B-VIII.0 evaluation [1]. The full energy range is shown in (a). For clarity, detailed views covering different energy ranges are shown in separate panels: (b) shows the threshold for first-chance fission, while the second-chance fission threshold is displayed in (c); the high energy range can be seen in (d).

Detailed views on different energy regions are also given: Figure 10(b) shows the region around fission threshold, where our data agree well with the ENDF/B-VIII.0 evaluation. The width of the binning used in our data is limited by the statistical uncertainty, whereas the intrinsic energy resolution of the experimental setup is much better. In any case, it is enough to reproduce the resonance structure that is present around the fission threshold of ^{232}Th. According to Sin *et al.* [7], the presence of such a complex structure in the cross section would be explained by the existence of a triple-humped fission barrier for light actinides [6].

Our data agree well with the experimental data from Shcherbakov *et al.* [54], who reported results up to 200 MeV. Results from Lisowski *et al.* [56] range only up to 20 MeV and show the same systematic discrepancy with our data as observed in the ratio $\sigma_f(^{232}$Th$)/\sigma_f(^{235}$U$)$. Recent values obtained with quasi-monoenergetic neutrons, done by Michalopoulou *et al.* [58] (in the range between 2 and 18 MeV) and by Gledenov *et al.* [57] (in different ranges around 5 and around 10 MeV), also agree well with our data.

Comparisons with several evaluations will be discussed in Section VII. The numerical results of the cross section $\sigma_f(^{232}$Th$)$ and of the ratio $\sigma_f(^{232}$Th$)/\sigma_f(^{235}$U$)$ are listed

in Table V (Appendix A), together with their statistical uncertainties.

B. ^{233}U(n, f)

The obtained ratio $\sigma_f(^{233}$U$)/\sigma_f(^{235}$U$)$ from 10 keV is shown in Fig. 11, compared to previous results [54,56,63,64] available in EXFOR [22]. The error bars in our data account for statistical uncertainties. Among the compared values, data from Shcherbakov *et al.* [54] and Tovesson *et al.* [64] agree with our results within statistical uncertainties in their whole energy range, whereas data from Lisowski *et al.* [56] overestimate our values between 50 and 200 MeV.

A good agreement, except for two points around 10 MeV, is also found with the data of Belloni *et al.* [63], that were measured, up to 20 MeV, using a fast ionization chamber (FIC) at the same experimental area at n_TOF.

The final result for $\sigma_f(^{233}$U$)$, ranging from 0.7 eV up to 1 GeV, is shown in Fig. 12, where the error bars in our data account for the statistical uncertainties only. Again, our results are the only ones covering such a broad energy range of the incident neutron.

The resolved resonance region (RRR) is displayed in Fig. 12(a), whereas Figs. 12(b) and 12(c) show the unresolved
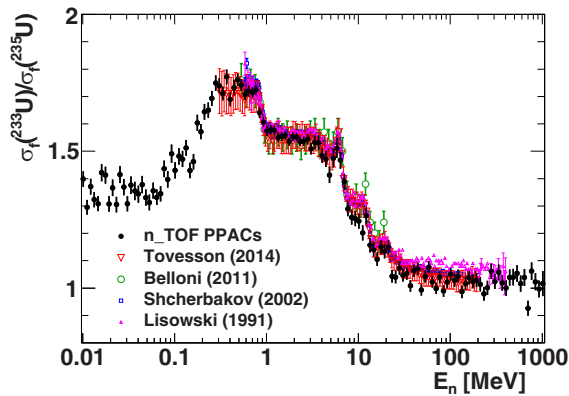
FIG. 11. Fission cross section ratio of ^{233}U relative to ^{235}U from 10 keV up to 1 GeV, compared with previous results [54,56,63,64]. The error bars in our data represent statistical uncertainties.

resonance region (URR). The detailed view in Fig. 12(e) shows how the n_TOF high energy resolution allows us to observe resonance structures above the current limit of the RRR at 600 eV, as reported earlier by Calviani *et al.* [66]. These observations confirm the results obtained by Guber *et al.* [65] and provide new data that can contribute to a possible extension of the evaluated resolved resonance region above that energy.

Figure 12(d) plots the high energy region, compared with previous results [54,63,64,66] available in the EXFOR database [22] and with the evaluation ENDF/B-VIII.0 [1]. The results from Manabe *et al.* [61] and Meadows *et al.* [62], using monoenergetic neutrons of 14.7 MeV, follow very closely the ENDF/B-VIII.0 evaluation and are omitted from the figure. The data set from Shcherbakov *et al.* [54] is the only one reaching neutron energies as high as 200 MeV, and the only discrepancies with our data arise above 100 MeV. It is worth pointing out that data from Calviani *et al.* [66], and Belloni *et al.* [63], covering different neutron energy ranges, were also measured at the same experimental area EAR1 at n_TOF, but using a fast ionization chamber (FIC). The use of the PPACs, equipped with fast anodes, and being less sensitive to the γ flash than the FIC setup, has made it possible to provide data with a higher energy resolution, as well as to extend the measurement of the ^{233}U(n, f) cross section up to 1 GeV.

Figure 12(f) shows a detailed view of the fission cross section at the lowest neutron energies available at n_TOF. It is interesting to note that the integral of the cross section between 8.1 and 14.7 eV is being discussed to become a secondary standard because of the good agreement between the existing experimental works [67]. These energy limits correspond to deep and flat valleys in the cross section, in such a way that the integral is rather independent on the energy calibration uncertainty.

The numerical results of the cross section $\sigma_f(^{233}$U$)$ and of the ratio $\sigma_f(^{233}$U$)/\sigma_f(^{235}$U$)$ above 10 keV are listed in Table VI (Appendix B), together with their statistical uncertainties.

VII. COMPARISON WITH EVALUATIONS

The final results of the fission cross section ratios $\sigma_f(^{232}$Th$)/\sigma_f(^{235}$U$)$ and $\sigma_f(^{233}$U$)/\sigma_f(^{235}$U$)$ are compared, in Fig. 13, with the latest versions of the major evaluation libraries: ENDF/B-VIII.0 [1], JENDL-5 [3], JEFF-3.3 [2], BROND-3.1 [68], and CENDL-3.2 [69]. The evaluation TENDL-2019 [70], based on the reaction code TALYS, is omitted from this comparison because its files for ^{233}U and ^{235}U (among some other isotopes) are taken directly from ENDF/B-VIII.0.

The figure shows the ratios between our experimental data and the evaluations, for the relative cross sections $\sigma_f(^{232}$Th$)/\sigma_f(^{235}$U$)$ and $\sigma_f(^{233}$U$)/\sigma_f(^{235}$U$)$, for energies above 1 MeV and 10 keV, respectively.

For both ^{232}Th and ^{233}U, our data reach higher neutron energies than current evaluations, since most of them stop at 20 MeV for both isotopes. Energies up to 30 MeV are reported only in ENDF/B-VIII.0 and JEFF-3.3 for ^{232}Th(n, f), whereas, for ^{233}U, only JEFF-3.3 extends up to 30 MeV.

A. ^{232}Th(n, f)

Figure 13(a) shows a good agreement between our results for $\sigma_f(^{232}$Th$)/\sigma_f(^{235}$U$)$ and the ENDF/B-VIII.0 and JEFF-3.3 evaluations, within uncertainties (with discrepancies of 1% in average). But they are systematically lower than JENDL-5 and CENDL-3.2 (7% and 5% in average, respectively). In the case of BROND-3.1 our data agree within 0.5% up to the second-chance fission (at ≈ 7 MeV) but are 5% lower than the evaluation at higher energies.

There is a remarkable discrepancy between our results and all the evaluations in one single point at 1.8 MeV. Figure 10(b) shows more clearly the difference in $\sigma_f(^{232}$Th$)$ for the case of the ENDF/B-VIII.0 evaluation. Since it is one single point that is not matching the evaluation, it does not seem to be caused by our choice of the energy intervals. That neutron energy corresponds to the region where the contribution of the angular efficiency correction is maximum. Therefore, it is possible that the experimental data on which the evaluations are based (mainly the data from Blons *et al.* [59]) do not properly take into account the effect of the angular distribution at that particular neutron energy. Moreover, experimental data on $\sigma_f(^{232}$Th$)$ from Meadows *et al.* [60] and from Shcherbakov *et al.* [54] also differ from the ENDF/B-VIII.0 evaluation and are compatible with our result at that energy, as seen in Fig. 10(b).

Smaller disagreements are found at the onsets of second- and third-chance fission thresholds (≈ 7 MeV and ≈ 13 MeV, respectively) and are compared to ENDF/B-VIII.0 also in Fig. 10(c). Given the low statistical uncertainty and the high-energy resolution of our data in that energy range, it seems that the disagreements are, in this case, caused by the too wide energy intervals of the evaluation.

B. ^{233}U(n, f)

At low energy, all the evaluations mentioned in the present article (ENDF/B-VIII.0, JENDL-5, JEFF-3.3, BROND-3.1,
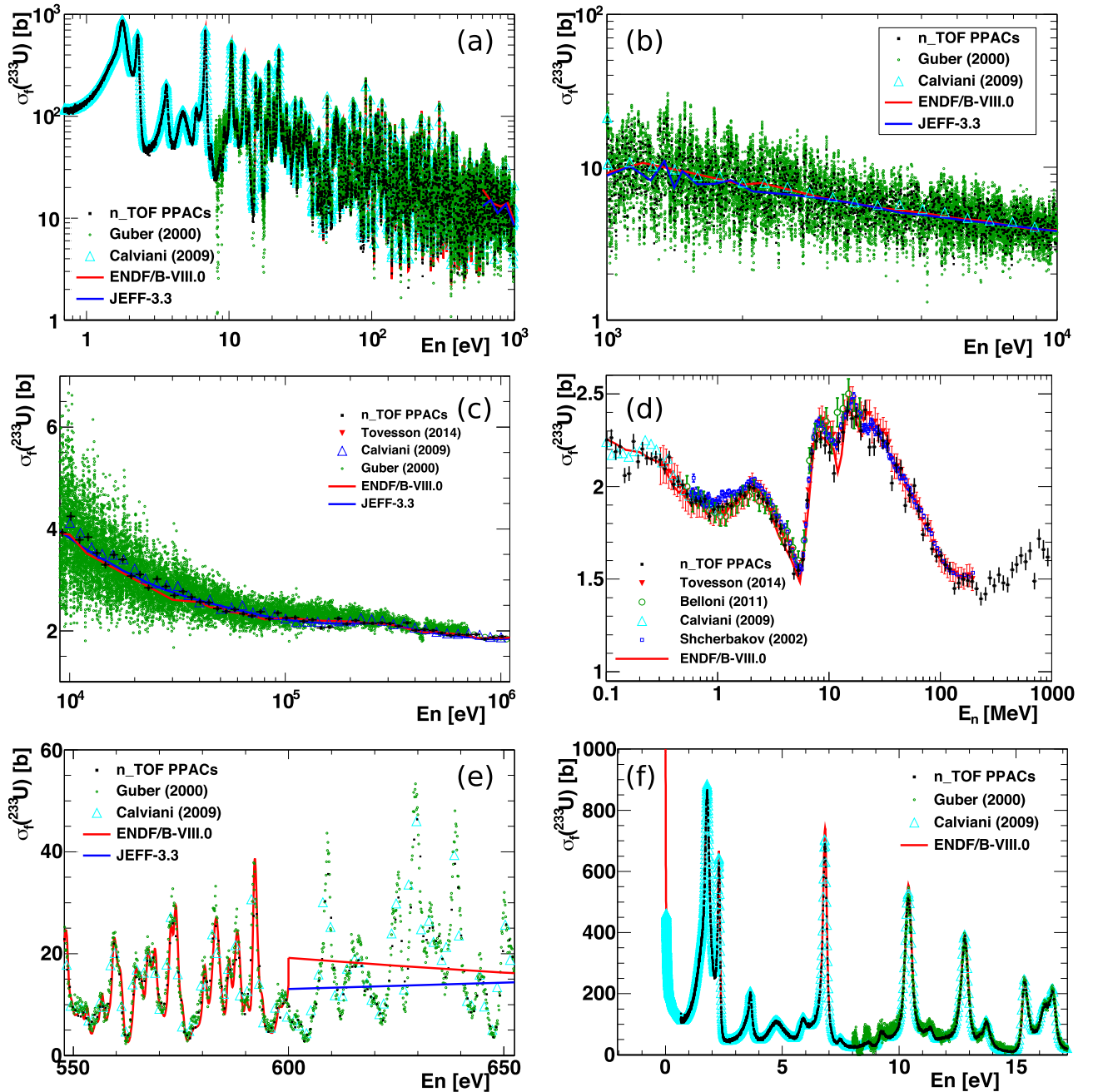
FIG. 12. Final cross section of ^{233}U(n, f) obtained in the present work. Previous experimental data [54,63–66] and evaluations [1,2] are shown for comparison. The low-energy resonance region can be seen in (a), and the URR in (b) and (c). The high-energy region, between 0.1 MeV and 1 GeV, is plotted in (d). Panel (e) shows a detailed view on the limit at 600 eV of the evaluated RRR. Panel (f) plots the lowest neutron energies available at n_TOF; the region 8.1–14.7 eV is being considered for an integral cross-section standard (see text for details).

and CENDL-3.2) share the same evaluation for the resolved resonance region of ^{233}U(n, f).

As mentioned in Sec. VI, the integral cross section between 8.1 and 14.7 eV could be suitable as a secondary standard and work is being done on the topic [67]. Our data give an integral of 660.2 b eV that is compatible, within uncertainties

($\pm 3.3\%$), with the value of 679.5 b eV obtained by integration of ENDF/B-VIII.0 values.

Figure 14 shows a comparison, for the region between 1 eV and 10 keV, between our data and the ENDF/B-VIII.0 evaluation by using the integral cross sections. There seems to be some trends in the energy dependence; it is worth noting
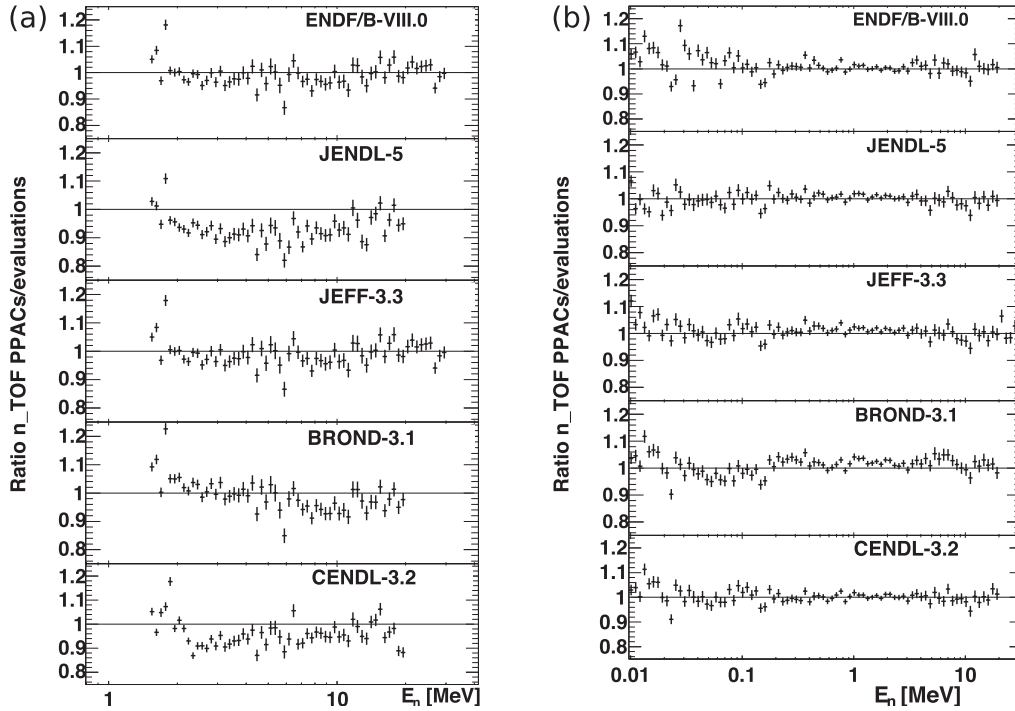
FIG. 13. Ratios between our data and evaluations from the major libraries [1–3,68,69] for the fission cross section ratios $\sigma_f(^{232}\text{Th})/\sigma_f(^{235}\text{U})$ (a) and $\sigma_f(^{233}\text{U})/\sigma_f(^{235}\text{U})$ (b).

the large discrepancies, up to 5%, around the limit between the resolved and unresolved resonance regions (at 600 eV).

Above 10 keV, the ratios between our results and the aforementioned evaluations are shown in Fig. 13(b). In the energy range between 10 keV and 1 MeV, our data differ by only 0.5% on average from the JENDL-5 evaluation, whereas the discrepancies with the other evaluations are within 2%. Concerning energies above 1 MeV, our data differ from ENDF/B-VIII.0, JENDL-5 and CENDL-3.2 by less than 2% on average, whereas the discrepancy amounts to 3% for JEFF-3.3 and 4% for BROND-3.1. The dependence on the neutron energy does not show, however, any remarkable trend.
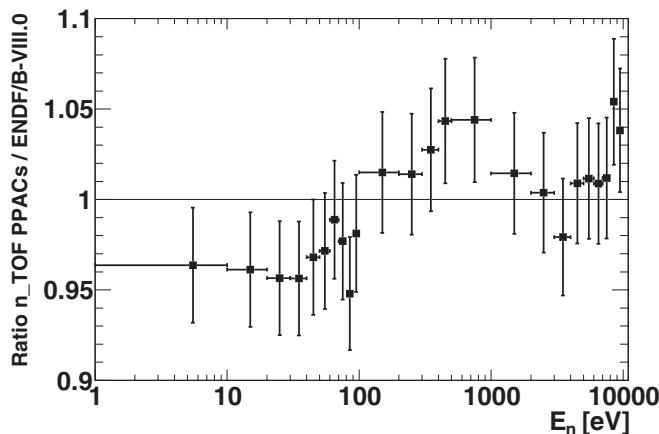
FIG. 14. Ratio between our data and the ENDF/B-VIII.0 evaluation [1] for $\sigma_f(^{233}\text{U})$ below 10 keV.

VIII. HIGH-ENERGY FISSION

Fission induced by nucleons at high energies (above $\approx$ 100 MeV), also called spallation-induced fission, is usually described by Monte Carlo methods as a three-stage process: First, the incident nucleon interacts with individual nucleons inside the target nucleus, producing a number of binary collisions that can eject some of these nucleons, or eject other nucleons, hence producing a fast intranuclear cascade. This is followed by a preequilibrium phase where the residual nucleus reaches a thermal equilibrium and, finally, decays via particle evaporation or fission. Some models, such as the Cascade Exciton Model (CEM03) [9] follow this procedure. However, it is even possible to skip the preequilibrium phase and replace it by a self-consistent calculation of the stopping time of the cascade [71], as is done in the Liège Intranuclear Cascade Model (INCL++) [8]. In this case, the whole process is reduced to only two phases: intra-nuclear cascade and fission-evaporation decay. The INCL++ output can be used in another code, such as abla07 [11] or GEMINI++ [12], to simulate the decay process of the equilibrated remnant resulting from the cascade.

A. Model calculations

In this work, we compare our experimental fission cross section data with model calculations using the combination of INCL++ (version 6.28) and ABLA07 to obtain the neutron-induced fission cross sections of ^{232}Th and ^{233}U above 200 MeV. Figures 15(a) and 15(b) show these theoretical results compared to the mentioned experimental data. The

FIG. 15. Our results on neutron-induced fission cross sections for ^{232}Th (a) and ^{233}U (b) are shown together with the calculated values from the combination of reaction codes INCL++ and ABLA07. Proton-induced data from Ref. [72] are also shown for comparison.

FIG. 16. Experimental data on fission cross section for proton- and neutron-induced fission, at 1 GeV nucleon energy, as a function of the fissility parameter of the target nucleus. Proton-induced data are from Kotov *et al.* [72]. The neutron-induced data include the present work and our earlier data obtained with PPACs at n_TOF [14–16], updated by using the ^{235}U cross section from Ref. [53] as reference, which is also included in the figure. The error bars include both statistical and systematic uncertainties.

data points are more spaced in the case of ^{233}U due to the lower statistics obtained with a single sample and a shorter beam time. In both figures, the green dashed lines c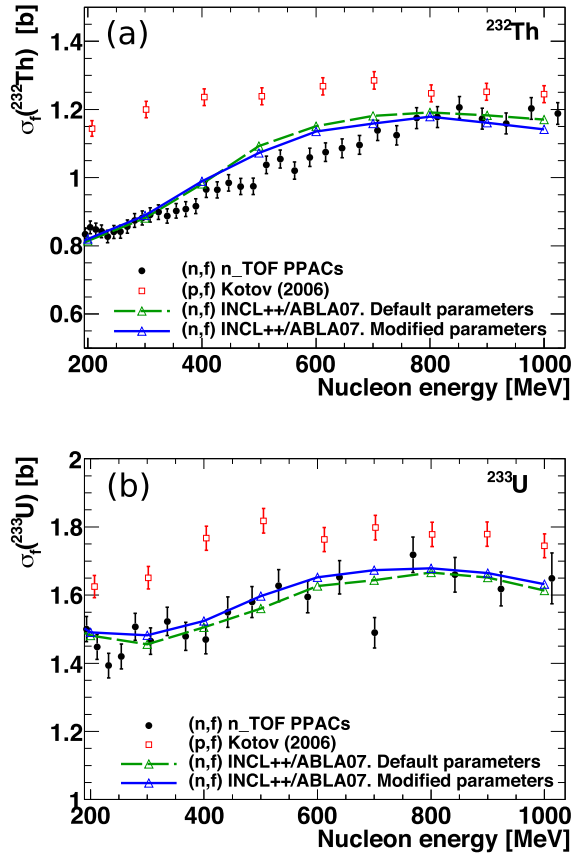orrespond to the (n, f) cross section obtained with the default set of parameters from INCL++ and ABLA07, which do not reproduce our experimental data. To try to improve the agreement with our experimental data, the values of some physical parameters of the decay code ABLA07 were modified, namely, the asymptotic level density parameter at the saddle point ($\tilde{a}_f$) and the height of the liquid-drop fission barrier (B_f), leading to the results shown by the solid blue lines.

In the case of ^{232}Th [Fig. 15(a)], INCL++/ABLA07 reproduces more closely our experimental data by decreasing ($\tilde{a}_f$) by 0.5% and reducing B_f by 0.1 MeV for all the fissioning remnants. For ^{233}U [Fig. 15(b)], a reduction of B_f by 0.1 MeV improves slightly the agreement with the data.

B. Comparison with (p, f)

It is known that at ≈ 100 MeV, the proton-induced fission cross section for a given nucleus is larger than the neutron-induced one [73]. The reason is that the fission cross section increases with the fissility parameter of the fissioning nucleus Z^2/A, that represents the competition between the Coulomb repulsion and the surface tension. For reactions

induced by high-energy nucleons, a fast intranuclear cascade takes place and the remnant nuclei follow a distribution of proton and mass numbers. In the case of (p, f) reactions, the remnants with proton number $Z_{\text{target}} + 1$, which are not achievable in the case of (n, f) reactions, contribute to increase the (p, f) cross section in comparison to the (n, f) cross section. Therefore, and despite the statistical nature of the emission of nucleons during the cascade, the remnant preserves some memory of the initial nucleus [74].

However, the difference between (p, f) and (n, f) decreases with the energy of the incoming nucleon, so that both cross sections are expected to be similar at ≈ 1 GeV. This behavior is confirmed by Fig. 15, where the experimental results from proton-induced fission obtained by Kotov *et al.* [72] are compared to our neutron data.

Apart from the measurement on ^{232}Th and ^{233}U reported here, several other actinides (^{234}U, ^{235}U, ^{238}U, ^{237}Np) and sub-actinides ($^{\text{nat}}$Pb, ^{209}Bi) have been studied at the n_TOF facility using the same experimental setup. In consequence, fission cross sections up to 1 GeV neutron energy have been already reported for all of them [14–16] except for ^{235}U, which was always used as the reference nucleus. Figure 16 shows the fission cross section at 1 GeV neutrons for all these isotopes, as a function of the fissility parameter of the target nucleus. For this plot, the neutron cross sections from earlier publications were recalculated by multiplying their reported ratios to ^{235}U by the same reference cross section for ^{235}U(n, f) as used in the present work, which is also included in the figure [53].

Our data clearly show an increase of the fission cross section with Z^2/A, as expected, but only up to ^{235}U, where it reaches saturation; available nuclei with higher fissility (^{234}U, ^{233}U, and ^{237}Np) show the same (n, f) cross section as ^{235}U. A similar behavior is observed in fission induced by 1 GeV protons, obtained by Kotov *et al.* [72], also shown in the

same figure. Again, some nuclei with a larger fissility than ^{235}U (in this case, ^{233}U, ^{237}Np, and ^{239}Pu) have a (p, f) cross section that is compatible, within error bars, with that of ^{235}U.

The authors of Ref. [72] claim, in their conclusions, that the fission cross section increases with Z^2/A up to ^{233}U and, in consequence, that there is a systematic rise of the fission cross section when coming from ^{238}U to lighter uranium isotopes. However, it can be seen in Fig. 16 that their data are also compatible, within their uncertainties, with a saturation of the cross section for nuclei beyond ^{235}U, as observed in our data with neutrons.

Moreover, one can also see from Fig. 16 that the saturation value of the cross section reached for ^{235}U is very similar for neutron- and proton-induced fission. This general behavior supports the idea that, at ≈ 1 GeV, neutron- and proton-induced fission cross sections are nearly the same.

It is worth pointing out that the authors of Ref. [51] attempted to reproduce the results from Kotov using the intranuclear cascade code INCL++, coupled to a different decay code than used here, GEMINI++. They could not find a solution that properly described the full behavior of the ^{233}U(p, f) cross section, while keeping physically reasonable values of the fission parameters.

Therefore, the discrepancy in the interpretation of the experimental results of ^{233}U, regarding the existence of a trend (as claimed by Kotov) or of a constant behavior of the fission cross section with the fissility parameter beyond ^{235}U (as we claim), together with the found difficulties in reproducing its proton-induced fission cross sections by theoretical models [51], suggest that more research must be done on this isotope. Further investigation on the existing nuclear reaction models, and on the influence of other model parameters on the cross section, might be needed to reproduce the particularities observed for ^{233}U.

The fact that only two measurements at those high energies exist (one with protons, and our one with neutrons) makes it difficult to understand if this discrepancy has a physical meaning, or if it is just a consequence of experimental uncertainties. Additional experimental measurements of the fission cross section induced by 1 GeV nucleons on ^{233}U and on other lighter uranium nuclei would provide useful information to determine the general behavior of uranium isotopes and, in particular, to explore the region of fissility where the fission cross section becomes saturated.

IX. SUMMARY AND CONCLUSIONS

The ^{232}Th(n, f) and ^{233}U(n, f) cross sections were measured with respect to ^{235}U(n, f) at the n_TOF facility up to 1 GeV, extending the knowledge of these cross sections up to higher neutron energies than ever before. The lowest neutron energies reported here are fission threshold and 0.7 eV, for ^{232}Th and ^{233}U, respectively. The fission events were identified by the detection in coincidence of both fission fragments using PPACs. The effect of the different angular distribution of the fission fragments was taken into account and, for the case of ^{232}Th, the FFAD measured in the same experiment was used.

The fission cross section ratios $\sigma_f(^{232}\mathrm{Th})/\sigma_f(^{235}\mathrm{U})$ and $\sigma_f(^{233}\mathrm{U})/\sigma_f(^{235}\mathrm{U})$ are provided. These ratios are not normalized to previous evaluations, thus they represent absolute results that will not be affected by future changes in the reference cross section of ^{235}U(n, f). In addition, these ratios were converted into cross sections by using the ^{235}U(n, f) cross section from the IAEA standard 2017 up to 200 MeV [49], and the ^{235}U(n, f) evaluation developed by Duran *et al.* above 200 MeV [53]. Results of the deduced fission cross sections $\sigma_f(^{232}\mathrm{Th})$ and $\sigma_f(^{233}\mathrm{U})$, and of their ratios with respect to ^{235}U will be submitted to the EXFOR database. The results were compared with previous experiments and with the major evaluated libraries.

The present work is expected to contribute to the improvement of the quality of upcoming versions of the evaluated cross sections, as well as to the extension of their range beyond the current limits. The high resolution data of ^{233}U could contribute to a better evaluation of the resolved and unresolved resonance regions, as well as to establishing a secondary standard for fission cross sections at low energies [67].

The data on the fission cross section of ^{232}Th presented here, together with the angular distribution of the emitted fragments published earlier [20,48], form a valuable set of data for the development of the existing parametrizations of the fission barrier for the actinides.

Fission induced by high-energy nucleons was discussed, and model calculations using INCL++/ABLA07 were performed on our (n, f) data. Modification of some parameters in the code was done to reproduce the results. Furthermore, our present data were compared with data from proton-induced fission up to 1 GeV. Data on other isotopes also measured at n_TOF with the same experimental setup, and together with the data on ^{232}Th and ^{233}U presented here, were used to study the dependence of the fission cross section with the fissility parameter Z^2/A of the target nucleus. It was shown that the fission cross section around 1 GeV reaches a saturated value for ^{235}U. In addition, our results also support the frequently used assumption that (p, f) and (n, f) cross sections are equal at ≈ 1 GeV.

Moreover, the present work can contribute to the development of the nuclear codes for reactions induced by high-energy nucleons. The analysis has pointed out some open questions regarding the differences between experimental data on (n, f) and (p, f) cross sections for ^{233}U at high energies, that call for further experiments on fission induced by high-energy nucleons on ^{233}U and on other light uranium isotopes, to explore the region of fissility where the fission cross section becomes saturated.

APPENDIX A: RESULTS FOR ^{232}Th(n, f)

Table V contains the complete set of numerical results obtained, in this work, for the fission cross section ratio $\sigma_f(^{232}\text{Th})/\sigma_f(^{235}\text{U})$ and for the deduced value of $\sigma_f(^{232}\text{Th})$. Both are given in the whole energy range from fission threshold and up to 1 GeV. These results are also shown, graphically, in Figs. 9 and 10.

TABLE V. Cross section ratio $\sigma_f(^{232}\text{Th})/\sigma_f(^{235}\text{U})$ and deduced value of $\sigma_f(^{232}\text{Th})$ as a function of the neutron energy. The errors indicate statistical uncertainties only. See Sec. V for a discussion on the systematic uncertainties.

E_n (MeV)	$\sigma_f(^{232}\text{Th})/\sigma_f(^{235}\text{U})$ (dimensionless)	$\sigma_f(^{232}\text{Th})$ (mb)
1.006	0.0016 ± 0.0003	1.9 ± 0.4
1.017	0.0023 ± 0.0004	2.7 ± 0.5
1.029	0.0012 ± 0.0003	1.5 ± 0.4
1.041	0.0016 ± 0.0003	2.0 ± 0.4
1.053	0.0017 ± 0.0003	2.0 ± 0.4
1.065	0.0023 ± 0.0004	2.7 ± 0.4
1.078	0.0026 ± 0.0004	3.1 ± 0.4
1.090	0.0025 ± 0.0004	3.0 ± 0.4
1.103	0.0023 ± 0.0004	2.7 ± 0.4
1.116	0.0031 ± 0.0004	3.7 ± 0.5
1.129	0.0029 ± 0.0004	3.5 ± 0.5
1.142	0.0026 ± 0.0004	3.1 ± 0.4
1.155	0.0030 ± 0.0004	3.6 ± 0.5
1.168	0.0036 ± 0.0005	4.4 ± 0.5
1.182	0.0040 ± 0.0005	4.8 ± 0.6
1.195	0.0052 ± 0.0005	6.3 ± 0.6
1.209	0.0048 ± 0.0005	5.8 ± 0.6
1.223	0.0075 ± 0.0006	9.0 ± 0.7
1.237	0.0083 ± 0.0007	10.0 ± 0.8
1.252	0.0082 ± 0.0007	9.9 ± 0.8
1.266	0.0103 ± 0.0007	12.5 ± 0.9
1.281	0.0158 ± 0.0010	19.2 ± 1.2
1.296	0.016 ± 0.001	19.7 ± 1.3
1.311	0.022 ± 0.001	26.2 ± 1.5
1.326	0.028 ± 0.001	34.4 ± 1.7
1.341	0.035 ± 0.002	42.5 ± 1.9
1.357	0.038 ± 0.002	46.6 ± 1.9
1.372	0.042 ± 0.002	51.4 ± 2.1
1.388	0.047 ± 0.002	57.5 ± 2.2
1.404	0.052 ± 0.002	64.3 ± 2.4
1.421	0.048 ± 0.002	59.5 ± 2.2
1.437	0.053 ± 0.002	65.0 ± 2.4
1.454	0.051 ± 0.002	63.0 ± 2.3
1.471	0.053 ± 0.002	66.2 ± 2.5
1.488	0.058 ± 0.002	72.5 ± 2.4
1.505	0.062 ± 0.002	77.3 ± 2.6
1.522	0.070 ± 0.002	86.9 ± 2.9
1.540	0.079 ± 0.002	98.8 ± 3.1
1.558	0.089 ± 0.003	111.4 ± 3.3
1.576	0.102 ± 0.003	127.5 ± 3.5
1.594	0.101 ± 0.003	127.1 ± 3.7
1.613	0.099 ± 0.003	124.7 ± 3.7
1.631	0.079 ± 0.002	99.3 ± 3.0
1.650	0.064 ± 0.002	80.4 ± 2.9

TABLE V. *(Continued.)*

E_n (MeV)	$\sigma_f(^{232}\text{Th})/\sigma_f(^{235}\text{U})$ (dimensionless)	$\sigma_f(^{232}\text{Th})$ (mb)
1.669	0.062 ± 0.002	78.3 ± 2.8
1.689	0.075 ± 0.002	94.9 ± 3.1
1.708	0.080 ± 0.003	101.4 ± 3.3
1.728	0.072 ± 0.003	91.2 ± 3.3
1.748	0.063 ± 0.002	79.4 ± 2.9
1.768	0.058 ± 0.002	73.2 ± 2.5
1.789	0.062 ± 0.002	79.5 ± 2.6
1.809	0.075 ± 0.002	95.2 ± 2.9
1.830	0.080 ± 0.003	101.5 ± 3.2
1.851	0.087 ± 0.003	110.8 ± 3.4
1.873	0.093 ± 0.003	119.5 ± 3.5
1.895	0.091 ± 0.003	116.6 ± 3.8
1.916	0.085 ± 0.003	108.5 ± 3.6
1.939	0.088 ± 0.003	113.1 ± 3.6
1.961	0.088 ± 0.003	113.6 ± 3.5
1.984	0.091 ± 0.003	117.7 ± 3.4
2.007	0.094 ± 0.003	121.6 ± 3.9
2.030	0.091 ± 0.003	116.9 ± 3.7
2.054	0.094 ± 0.003	121.3 ± 3.9
2.077	0.094 ± 0.003	121.0 ± 3.8
2.101	0.101 ± 0.003	130.0 ± 4.0
2.126	0.099 ± 0.003	127.4 ± 3.8
2.150	0.102 ± 0.003	130.8 ± 4.0
2.175	0.106 ± 0.003	135.8 ± 4.2
2.200	0.105 ± 0.003	134.5 ± 4.1
2.226	0.104 ± 0.003	133.1 ± 4.0
2.252	0.098 ± 0.003	125.6 ± 3.9
2.278	0.091 ± 0.003	116.3 ± 3.9
2.304	0.087 ± 0.003	110.5 ± 3.7
2.331	0.090 ± 0.003	113.9 ± 3.7
2.358	0.082 ± 0.003	103.8 ± 3.3
2.385	0.089 ± 0.003	113.1 ± 3.7
2.413	0.091 ± 0.003	115.4 ± 3.9
2.441	0.087 ± 0.003	109.4 ± 3.5
2.469	0.088 ± 0.003	111.7 ± 3.7
2.498	0.095 ± 0.003	119.3 ± 4.2
2.526	0.092 ± 0.003	115.5 ± 4.0
2.571	0.091 ± 0.002	115.0 ± 2.1
2.692	0.097 ± 0.002	121.4 ± 2.2
2.819	0.105 ± 0.002	129.7 ± 2.4
2.952	0.105 ± 0.002	128.1 ± 2.5
3.091	0.113 ± 0.002	136.3 ± 2.7
3.237	0.110 ± 0.002	131.2 ± 2.9
3.389	0.114 ± 0.003	134.7 ± 3.1
3.549	0.118 ± 0.003	138.1 ± 3.3
3.716	0.120 ± 0.003	139.1 ± 3.5
3.891	0.125 ± 0.003	143.6 ± 3.6
4.075	0.124 ± 0.003	141.2 ± 3.5
4.267	0.131 ± 0.003	147.9 ± 3.9
4.468	0.119 ± 0.003	133.0 ± 3.6
4.679	0.134 ± 0.004	147.4 ± 4.0
4.899	0.130 ± 0.004	140.3 ± 4.0
5.130	0.140 ± 0.004	149.5 ± 4.4
5.372	0.138 ± 0.004	145.4 ± 4.3
5.625	0.132 ± 0.004	137.1 ± 4.3
5.890	0.123 ± 0.004	130.7 ± 4.0

TABLE V. (*Continued.*)

E_n (MeV)	$\sigma_f(^{232}\text{Th})/\sigma_f(^{235}\text{U})$ (dimensionless)	$\sigma_f(^{232}\text{Th})$ (mb)
6.168	0.155 ± 0.004	180.8 ± 5.1
6.458	0.214 ± 0.005	280.8 ± 7.2
6.763	0.239 ± 0.006	345.3 ± 8.3
7.081	0.240 ± 0.006	375.9 ± 8.7
7.415	0.232 ± 0.005	388.9 ± 9.1
7.765	0.207 ± 0.005	361.0 ± 8.5
8.130	0.198 ± 0.005	354.7 ± 8.5
8.514	0.188 ± 0.005	337.7 ± 8.2
8.915	0.182 ± 0.005	323.4 ± 8.1
9.335	0.177 ± 0.005	314.4 ± 8.0
9.775	0.182 ± 0.005	321.4 ± 8.3
10.24	0.174 ± 0.005	304.5 ± 8.1
10.72	0.174 ± 0.005	303.1 ± 8.2
11.22	0.169 ± 0.005	290.3 ± 8.0
11.75	0.184 ± 0.005	315.4 ± 9.0
12.31	0.176 ± 0.005	311.3 ± 8.6
12.89	0.162 ± 0.005	302.5 ± 8.5
13.49	0.157 ± 0.004	311.3 ± 8.5
14.13	0.173 ± 0.005	361.1 ± 9.4
14.80	0.189 ± 0.005	399.4 ± 10.1
15.49	0.217 ± 0.005	464.0 ± 11.5
16.22	0.210 ± 0.005	448.9 ± 10.9
16.99	0.228 ± 0.006	478.0 ± 11.7
17.79	0.245 ± 0.006	506.7 ± 12.4
18.63	0.236 ± 0.006	481.9 ± 11.7
19.50	0.247 ± 0.006	500.5 ± 12.2
20.42	0.277 ± 0.007	568.3 ± 13.4
21.39	0.312 ± 0.007	655.2 ± 14.9
22.39	0.327 ± 0.007	695.2 ± 15.6
23.45	0.338 ± 0.007	717.2 ± 15.9
24.55	0.340 ± 0.007	717.7 ± 15.6
25.71	0.335 ± 0.007	712.1 ± 15.6
26.92	0.311 ± 0.007	655.5 ± 14.3
28.19	0.328 ± 0.007	697.8 ± 15.1
29.52	0.346 ± 0.007	738.3 ± 15.8
30.91	0.355 ± 0.007	761.7 ± 15.9
32.37	0.395 ± 0.008	844.3 ± 17.6
33.89	0.377 ± 0.008	798.2 ± 16.3
35.49	0.397 ± 0.008	815.8 ± 16.6
37.16	0.417 ± 0.008	835.1 ± 16.9
38.91	0.423 ± 0.008	840.9 ± 16.7
40.75	0.442 ± 0.009	878.5 ± 17.3
42.67	0.440 ± 0.009	867.5 ± 17.1
44.68	0.455 ± 0.009	891.1 ± 17.6
46.79	0.466 ± 0.009	904.5 ± 17.6
48.99	0.495 ± 0.010	944.8 ± 18.5
51.30	0.498 ± 0.010	948.6 ± 18.4
53.72	0.494 ± 0.009	926.5 ± 17.7
56.25	0.507 ± 0.010	957.5 ± 18.4
58.90	0.517 ± 0.010	963.8 ± 18.5
61.68	0.495 ± 0.009	912.0 ± 17.2
64.58	0.499 ± 0.009	910.4 ± 17.1
67.63	0.532 ± 0.010	945.6 ± 18.0
70.81	0.528 ± 0.010	919.5 ± 17.5
74.15	0.533 ± 0.010	924.5 ± 17.6
77.65	0.550 ± 0.011	950.6 ± 18.3
81.30	0.528 ± 0.010	900.0 ± 17.1

TABLE V. (*Continued.*)

E_n (MeV)	$\sigma_f(^{232}\text{Th})/\sigma_f(^{235}\text{U})$ (dimensionless)	$\sigma_f(^{232}\text{Th})$ (mb)
85.14	0.556 ± 0.011	934.2 ± 17.9
89.15	0.527 ± 0.010	856.0 ± 16.3
93.35	0.548 ± 0.011	870.9 ± 16.8
97.75	0.544 ± 0.011	854.2 ± 16.6
102.4	0.538 ± 0.010	834.4 ± 16.1
107.2	0.564 ± 0.011	869.2 ± 17.1
112.2	0.559 ± 0.011	857.7 ± 17.1
117.5	0.554 ± 0.011	836.8 ± 16.7
123.1	0.564 ± 0.011	841.4 ± 17.1
128.9	0.563 ± 0.011	831.3 ± 16.8
134.9	0.574 ± 0.012	843.3 ± 17.3
141.3	0.573 ± 0.012	831.7 ± 17.2
148.0	0.561 ± 0.012	816.0 ± 16.8
154.9	0.574 ± 0.012	838.5 ± 17.6
162.2	0.545 ± 0.011	787.8 ± 16.2
169.9	0.576 ± 0.012	830.7 ± 17.6
177.9	0.587 ± 0.013	854.4 ± 18.4
186.3	0.592 ± 0.013	859.4 ± 18.6
195.0	0.572 ± 0.012	826.5 ± 17.8
204.2	0.596 ± 0.013	854.1 ± 18.7
213.9	0.594 ± 0.013	848.0 ± 18.7
223.9	0.591 ± 0.013	842.2 ± 18.7
234.5	0.582 ± 0.013	827.2 ± 18.4
245.5	0.592 ± 0.013	840.7 ± 19.0
257.1	0.593 ± 0.013	841.4 ± 18.9
269.2	0.604 ± 0.014	856.6 ± 19.6
281.9	0.616 ± 0.014	874.5 ± 20.2
295.2	0.618 ± 0.014	881.5 ± 20.4
309.1	0.623 ± 0.015	890.4 ± 20.9
323.7	0.626 ± 0.015	898.8 ± 21.2
338.9	0.617 ± 0.015	887.5 ± 20.9
354.9	0.625 ± 0.015	902.5 ± 21.3
371.6	0.626 ± 0.015	908.0 ± 21.7
389.1	0.628 ± 0.015	916.3 ± 21.8
407.5	0.657 ± 0.016	965.3 ± 23.4
426.7	0.651 ± 0.016	964.2 ± 23.5
446.8	0.660 ± 0.016	984.4 ± 24.2
467.9	0.647 ± 0.016	974.1 ± 23.8
489.9	0.642 ± 0.016	974.7 ± 23.9
513.0	0.677 ± 0.017	1037.4 ± 25.9
537.2	0.683 ± 0.017	1054.6 ± 26.3
562.5	0.656 ± 0.016	1020.5 ± 25.2
589.0	0.676 ± 0.017	1059.5 ± 26.7
616.8	0.681 ± 0.017	1075.1 ± 27.2
645.8	0.683 ± 0.017	1086.2 ± 27.4
676.3	0.685 ± 0.017	1096.0 ± 27.7
708.1	0.708 ± 0.018	1138.6 ± 29.6
741.5	0.697 ± 0.018	1124.4 ± 28.4
776.5	0.726 ± 0.019	1174.7 ± 30.5
813.0	0.727 ± 0.019	1177.8 ± 30.6
851.4	0.744 ± 0.020	1206.3 ± 32.0
891.5	0.723 ± 0.019	1173.0 ± 31.0
933.5	0.714 ± 0.019	1159.0 ± 30.5
977.5	0.741 ± 0.020	1203.0 ± 32.2
1024	0.732 ± 0.020	1188.1 ± 31.9

APPENDIX B: RESULTS FOR ^{233}U(n, f)

Table VI contains the numerical results obtained, in this work, for the fission cross section ratio $\sigma_f(^{233}\text{U})/\sigma_f(^{235}\text{U})$ and for the deduced value of $\sigma_f(^{233}U)$, for neutron energies from 10 keV up to 1 GeV. These results are plotted in Figs. 11 and 12.

TABLE VI. Cross section ratio $\sigma_f(^{233}\text{U})/\sigma_f(^{235}\text{U})$ and deduced value of $\sigma_f(^{233}\text{U})$ as a function of the neutron energy. The errors indicate statistical uncertainties only. See Sec. V for a discussion on the systematic uncertainties.

E_n (MeV)	$\sigma_f(^{233}\text{U})/\sigma_f(^{235}\text{U})$ (dimensionless)	$\sigma_f(^{233}\text{U})$ (mb)
0.01013	1.398 ± 0.029	4246.4 ± 86.8
0.01110	1.295 ± 0.027	3787.8 ± 79.4
0.01217	1.371 ± 0.029	3840.3 ± 81.6
0.01335	1.323 ± 0.028	3528.4 ± 74.5
0.01464	1.309 ± 0.028	3295.7 ± 69.8
0.01605	1.422 ± 0.031	3493.2 ± 76.8
0.01760	1.413 ± 0.031	3402.2 ± 74.0
0.01930	1.308 ± 0.028	3077.8 ± 66.9
0.02116	1.367 ± 0.030	3108.7 ± 69.1
0.02320	1.305 ± 0.029	2846.2 ± 62.2
0.02544	1.415 ± 0.031	3016.7 ± 66.6
0.02789	1.369 ± 0.030	2872.2 ± 62.6
0.03058	1.309 ± 0.028	2695.9 ± 58.2
0.03353	1.376 ± 0.032	2773.1 ± 64.4
0.03677	1.355 ± 0.034	2664.2 ± 65.9
0.04031	1.344 ± 0.031	2568.5 ± 59.9
0.04420	1.379 ± 0.032	2553.5 ± 58.5
0.04847	1.331 ± 0.030	2437.6 ± 54.3
0.05314	1.313 ± 0.029	2380.8 ± 52.5
0.05827	1.356 ± 0.029	2420.5 ± 52.4
0.06389	1.332 ± 0.028	2331.6 ± 49.7
0.07006	1.345 ± 0.028	2291.9 ± 48.2
0.07682	1.436 ± 0.030	2375.9 ± 49.7
0.08423	1.397 ± 0.031	2239.6 ± 49.2
0.09236	1.491 ± 0.034	2350.2 ± 53.0
0.1013	1.430 ± 0.030	2250.9 ± 46.8
0.1110	1.482 ± 0.030	2263.5 ± 46.2
0.1217	1.472 ± 0.030	2187.2 ± 43.9
0.1335	1.513 ± 0.029	2214.5 ± 41.9
0.1464	1.430 ± 0.028	2058.9 ± 40.9
0.1605	1.462 ± 0.028	2069.1 ± 40.2
0.1760	1.604 ± 0.030	2243.0 ± 41.4
0.1930	1.572 ± 0.028	2134.3 ± 37.6
0.2116	1.644 ± 0.029	2201.8 ± 38.7
0.2320	1.651 ± 0.028	2152.1 ± 36.4
0.2544	1.693 ± 0.028	2150.2 ± 35.0
0.2789	1.749 ± 0.028	2157.9 ± 34.3
0.3058	1.739 ± 0.027	2144.5 ± 33.5
0.3353	1.711 ± 0.025	2095.5 ± 30.9
0.3677	1.772 ± 0.027	2159.2 ± 32.6
0.4031	1.690 ± 0.025	2012.6 ± 30.1
0.4420	1.732 ± 0.029	2026.4 ± 33.9
0.4847	1.761 ± 0.022	2009.8 ± 25.6
0.5314	1.742 ± 0.021	1960.0 ± 24.0

TABLE VI. *(Continued.)*

E_n (MeV)	$\sigma_f(^{233}\text{U})/\sigma_f(^{235}\text{U})$ (dimensionless)	$\sigma_f(^{233}\text{U})$ (mb)
0.5827	1.707 ± 0.021	1913.1 ± 23.0
0.6389	1.720 ± 0.020	1925.1 ± 22.5
0.7006	1.715 ± 0.020	1919.9 ± 21.8
0.7682	1.724 ± 0.019	1932.5 ± 21.4
0.8423	1.641 ± 0.019	1839.0 ± 21.4
0.9236	1.606 ± 0.018	1876.7 ± 21.4
1.013	1.574 ± 0.020	1890.2 ± 23.8
1.110	1.579 ± 0.017	1889.9 ± 20.5
1.217	1.576 ± 0.016	1905.3 ± 19.4
1.335	1.550 ± 0.017	1894.7 ± 20.3
1.464	1.554 ± 0.016	1924.5 ± 19.3
1.605	1.558 ± 0.015	1959.0 ± 19.2
1.760	1.535 ± 0.016	1951.6 ± 20.0
1.930	1.554 ± 0.016	1996.6 ± 20.5
2.116	1.552 ± 0.016	1990.8 ± 21.0
2.320	1.536 ± 0.017	1950.4 ± 21.0
2.544	1.537 ± 0.018	1933.9 ± 22.1
2.789	1.544 ± 0.020	1911.1 ± 24.4
3.058	1.509 ± 0.021	1824.7 ± 25.2
3.353	1.531 ± 0.025	1812.1 ± 29.4
3.677	1.531 ± 0.027	1771.3 ± 31.5
4.031	1.484 ± 0.027	1683.6 ± 30.6
4.420	1.472 ± 0.029	1647.2 ± 32.9
4.847	1.413 ± 0.029	1529.4 ± 31.9
5.314	1.474 ± 0.033	1548.3 ± 34.9
5.827	1.511 ± 0.035	1605.4 ± 37.6
6.389	1.468 ± 0.032	1926.5 ± 42.0
7.006	1.388 ± 0.028	2177.8 ± 44.3
7.682	1.289 ± 0.026	2244.3 ± 45.9
8.423	1.258 ± 0.026	2254.5 ± 47.0
9.236	1.254 ± 0.027	2222.1 ± 47.9
10.13	1.245 ± 0.028	2183.5 ± 48.6
11.10	1.202 ± 0.028	2069.9 ± 47.9
12.17	1.265 ± 0.030	2240.7 ± 53.1
13.35	1.158 ± 0.027	2293.3 ± 53.4
14.64	1.141 ± 0.026	2408.1 ± 54.1
16.05	1.105 ± 0.025	2367.1 ± 53.1
17.60	1.150 ± 0.026	2378.1 ± 53.4
19.30	1.135 ± 0.026	2300.4 ± 52.4
21.16	1.150 ± 0.026	2412.4 ± 54.8
23.20	1.044 ± 0.023	2212.2 ± 48.7
25.44	1.040 ± 0.023	2213.2 ± 48.3
27.89	1.073 ± 0.024	2284.7 ± 50.1
30.58	1.047 ± 0.023	2248.5 ± 48.7
33.53	1.053 ± 0.023	2231.5 ± 48.0
36.77	1.008 ± 0.022	2017.9 ± 43.1
40.31	1.064 ± 0.022	2115.3 ± 44.7
44.20	1.070 ± 0.023	2098.2 ± 44.5
48.47	0.993 ± 0.021	1897.1 ± 39.5
53.14	1.042 ± 0.022	1953.6 ± 40.8
58.27	1.076 ± 0.022	2004.1 ± 41.9
63.89	1.023 ± 0.022	1867.2 ± 39.5
70.06	0.999 ± 0.021	1740.5 ± 36.5
76.82	1.040 ± 0.022	1795.4 ± 37.7
84.23	0.990 ± 0.021	1663.8 ± 35.5
92.36	1.022 ± 0.022	1623.9 ± 35.1

TABLE VI. (*Continued.*)

E_n (MeV)	$\sigma_f(^{233}\text{U})/\sigma_f(^{235}\text{U})$ (dimensionless)	$\sigma_f(^{233}\text{U})$ (mb)
101.3	1.050 ± 0.023	1627.8 ± 35.5
111.0	1.029 ± 0.023	1577.1 ± 35.4
121.7	1.044 ± 0.024	1556.7 ± 35.1
133.5	0.986 ± 0.023	1449.5 ± 33.3
146.4	1.016 ± 0.024	1478.1 ± 34.9
160.5	1.038 ± 0.025	1499.8 ± 35.7
176.0	1.024 ± 0.025	1491.6 ± 35.7
193.0	1.029 ± 0.025	1486.5 ± 36.7
211.6	1.014 ± 0.026	1447.9 ± 36.7
232.0	0.979 ± 0.025	1393.2 ± 35.9
254.4	1.001 ± 0.026	1419.8 ± 36.7
278.9	1.061 ± 0.028	1507.2 ± 39.5
305.8	1.024 ± 0.027	1465.0 ± 39.2
335.3	1.058 ± 0.029	1522.7 ± 41.5

TABLE VI. (*Continued.*)

E_n (MeV)	$\sigma_f(^{233}\text{U})/\sigma_f(^{235}\text{U})$ (dimensionless)	$\sigma_f(^{233}\text{U})$ (mb)
367.7	1.019 ± 0.028	1479.0 ± 41.2
403.1	1.000 ± 0.028	1469.3 ± 41.3
442.0	1.039 ± 0.030	1549.9 ± 44.6
484.7	1.040 ± 0.030	1579.6 ± 45.5
531.4	1.054 ± 0.030	1627.7 ± 46.8
582.7	1.017 ± 0.030	1594.5 ± 46.5
638.9	1.039 ± 0.031	1652.2 ± 48.7
700.6	0.926 ± 0.028	1489.6 ± 44.7
768.2	1.062 ± 0.032	1718.4 ± 52.1
842.3	1.023 ± 0.031	1659.7 ± 50.6
923.5	0.997 ± 0.031	1618.3 ± 49.7
1013	1.017 ± 0.046	1649.4 ± 74.7

[1] D. Brown, M. Chadwick, R. Capote *et al.*, ENDF/B-VIII.0: The 8th major release of the Nuclear Reaction Data Library with CIELO-project cross sections, new standards and thermal scattering data, Nucl. Data Sheets **148**, 1 (2018), Special Issue on Nuclear Reaction Data.

[2] A. J. M. Plompen, O. Cabellos, C. De Saint Jean *et al.*, The joint evaluated fission and fusion nuclear data library, JEFF-3.3, Eur. Phys. J. A **56**, 181 (2020).

[3] O. Iwamoto, N. Iwamoto, K. Shibata *et al.*, Status of JENDL, EPJ Web Conf. **239**, 09002 (2020).

[4] International Atomic Energy Agency, Thorium fuel cycle - Potential benefits and challenges, IAEA-TECDOC No. 1450, 2005 (unpublished).

[5] S. Bjørnholm and J. E. Lynn, The double-humped fission barrier, Rev. Mod. Phys. **52**, 725 (1980).

[6] C. Wagemans, *The Nuclear Fission Process* (CRC, Boca Raton, FL, 1991)

[7] M. Sin, R. Capote, A. Ventura, M. Herman, and P. Obložinský́, Fission of light actinides: ^{232}Th(n, f) and ^{231}Pa(n, f) reactions, Phys. Rev. C **74**, 014608 (2006).

[8] A. Boudard, J. Cugnon, J. C. David, S. Leray, and D. Mancusi, New potentialities of the Liège intranuclear cascade model for reactions induced by nucleons and light charged particles, Phys. Rev. C **87**, 014606 (2013).

[9] S. G. Mashnik, K. K. Gudima, R. E. Prael *et al.*, CEM03.03 and LAQGSM03.03 event generators for the MCNP6, MC-NPX, and MARS15 transport codes, in *Proceedings of the Joint ICTP-IAEA Advanced Workshop on Model Codes for Spallation Reactions*, ICTP Trieste, Italy, 4-8 February 2008, INDC(NDS)-530 (IAEA, Vienna, 2008), p. 51.

[10] Y. Yariv and Z. Fraenkel, Intranuclear cascade calculation of high energy heavy ion collisions: Effect of interactions between cascade particles, Phys. Rev. C **24**, 488 (1981).

[11] A. Kelic, M. V. Ricciardi, and K.-H. Schmidt, ABLA07 - towards a complete description of the decay channels of a nuclear system from spontaneous fission to multifragmentation, in *Proceedings of the Joint ICTP-IAEA Advanced Workshop on Model Codes for Spallation Reactions*, ICTP Trieste, Italy, 4–8 February 2008, INDC(NDS)-530 (IAEA, Vienna, 2008), p. 181.

[12] R. J. Charity, GEMINI A code to simulate the decay of a compound nucleus by a series of binary decays, in *Proceedings of the Joint ICTP-IAEA Advanced Workshop on Model Codes for Spallation Reactions*, ICTP Trieste, Italy, 4–8 February 2008, INDC(NDS)-530 (IAEA, Vienna, 2008), p. 139.

[13] Benlliure, J. and Rodríguez-Sánchez, J. L., Spallation-induced fission reactions, Eur. Phys. J. Plus **132**, 120 (2017).

[14] C. Paradela, L. Tassan-Got, L. Audouin *et al.* (n_TOF Collaboration), Neutron-induced fission cross section of ^{234}U and ^{237}Np measured at the CERN Neutron Time-of-Flight (n_TOF) facility, Phys. Rev. C **82**, 034601 (2010).

[15] D. Tarrío, L. Tassan-Got, L. Audouin *et al.* (n_TOF Collaboration), Neutron-induced fission cross section of ^{nat}Pb and ^{209}Bi from threshold to 1 GeV: An improved parametrization, Phys. Rev. C **83**, 044620 (2011).

[16] C. Paradela, M. Calviani, D. Tarrío *et al.* (n_TOF Collaboration), High-accuracy determination of the ^{238}U / ^{235}U fission cross section ratio up to $\simeq 1$ GeV at n_TOF at CERN, Phys. Rev. C **91**, 024602 (2015).

[17] N. Colonna, A. Tsinganis, R. Vlastou *et al.*, The fission experimental programme at the CERN n_TOF facility: Status and perspectives, Eur. Phys. J. A **56**, 48 (2020).

[18] C. Guerrero, A. Tsinganis, E. Berthoumieux *et al.* (n_TOF Collaboration), Performance of the neutron time-of-flight facility n_TOF at CERN, Eur. Phys. J. A **49**, 27 (2013).

[19] M. Barbagallo, C. Guerrero, A. Tsinganis, D. Tarrío *et al.* (n_TOF Collaboration), High-accuracy determination of the neutron flux at n_TOF, Eur. Phys. J. A **49**, 156 (2013).

[20] D. Tarrío, L. Leong, L. Audouin *et al.* (n_TOF Collaboration), Measurement of the angular distribution of fission fragments using a PPAC assembly at CERN n_TOF, Nucl. Instrum. Methods Phys. Res., Sect. A **743**, 79 (2014).

[21] D. Tarrío, L. Tassan-Got, L. Audouin *et al.* (n_TOF Collaboration), On the systematic errors of the Th232(n,f) cross section measured with PPACs at CERN-n_TOF, in *Proceedings of the Final Scientific EFNUDAT Workshop, August 30 – September 2, 2010* (CERN, Geneva, 2010), p. 39.

[22] N. Otuka, E. Dupont, V. Semkova *et al.*, Towards a more complete and accurate experimental Nuclear Reaction Data Library

(EXFOR): International collaboration between Nuclear Reaction Data Centres (NRDC), Nucl. Data Sheets **120**, 272 (2014).

[23] A. S. Vorobyev, A. M. Gagarski, O. A. Shcherbakov, L. A. Vaishnene, and A. L. Barabanov, Angular distributions and anisotropy of the fragments from neutron-induced fission of ^{233}U and ^{209}Bi in the intermediate energy range of 1–200 MeV, JETP Lett. **104**, 365 (2016).

[24] K. D. Androsenko, G. G. Korolev, and D. L. Shpak, Angular anisotropy of fission fragments of ^{232}Th, ^{233}U, ^{235}U by neutrons with 12.4–16.4 MeV, Report No. INDC(CCP) **193**, 9 (1982).

[25] G. D.L.Shpak, Structure of the angular anisotropy and of the fission cross section of U-233, Sov. J. Nucl. Phys. **21**, 363 (1975).

[26] R. H. Iyer and M. L. Sagu, Fragment angular distributions in the 14 MeV neutron induced fission of Th232, U233, U235, U238, Np237, Pu239, Am241, B.A.R.C., Trombay Rep. Ser. **628**, 98 (1972).

[27] V. G. Nesterov, G. N. Smirenkin, and D. L. Shpak, Energy dependence of the fragment distribution in neutron fission of U-233,U-235 and Pu-239, Sov. J. Nucl. Phys. **4**, 713 (1967).

[28] R. B. Leachman and L. Blumberg, Fragment anisotropies in neutron-, deuteron-, and alpha-particle-induced fission, Phys. Rev. **137**, B814 (1965).

[29] J. E. Simmons and R. L. Henkel, Angular distribution of fragments in fission induced by MeV neutrons, Phys. Rev. **120**, 198 (1960).

[30] L. Blumberg and R. B. Leachman, Angular distributions of fragments from neutron-induced fission of ^{233}U and ^{239}Pu, Phys. Rev. **116**, 102 (1959).

[31] J. E. Brolley and W. C. Dickinson, Angular distribution of fragments from neutron-induced fission, Phys. Rev. **94**, 640 (1954).

[32] V. Geppert-Kleinrath, F. Tovesson, J. S. Barrett *et al.* (NIFFTE Collaboration 2), Fission fragment angular anisotropy in neutron-induced fission of ^{235}U measured with a time projection chamber, Phys. Rev. C **99**, 064619 (2019).

[33] S. A. Vorobyev, A. M. Gagarski, O. A. Shcherbakov, L. A. Vaishnene, and A. L. Barabanov, Angular distributions and anisotropy of fission fragments from neutron-induced fission in intermediate energy range 1–200 MeV, EPJ Web Conf. **146**, 04011 (2017).

[34] S. Ouichaoui, S. Juhasz, M. Varnagy, and J. Csikai, Angular distribution of fission fragments from U-235, U-238 and Np-237 near the (n,2nf) threshold, Acta Phys. Hung. **64**, 209 (1988).

[35] K. D. Androsenko, G. G. Korolev, and D. L. Shpak, The angular anisotropy of fragments of ^{235}U fission induced by 0.014–7.15 MeV neutrons, Report No. INDC(CCP) **292**, 11 (1989).

[36] M. Mahdavi, G. F. Knoll, and J. C. Robertson, Measurements of the 14 MeV fission cross-sections for ^{235}U and ^{239}Pu, in *Proceedings of the Conference on Nuclear Data For Science and Technology, Antwerp, 1982* (Reidel, Dordrecht, 1983), p. 58.

[37] J. W. Meadows and C. Budtz-Jorgensen, The fission fragment angular distributions and total kinetic energies for ^{235}U(n, f) from 0.18 to 8.83 MeV, in *Proceedings of the Conference on Nuclear Data For Science and Technology, Antwerp, 1982* (Reidel, Dordrecht, 1983), p. 740.

[38] S. Ahmad, M. M. Islam, A. H. Khan, M. Khaliquzzaman, M. Husain, and M. A. Rahman, The Energy dependence of fission fragment anisotropy in fast-neutron-induced fission of uranium-235, Nucl. Sci. Eng. **71**, 208 (1979).

[39] S. T. Hsue, G. F. Knoll, and J. Meadows, Angular distribution of fission fragments from fast fission of uranium-235, Nucl. Sci. Eng. **66**, 24 (1978).

[40] J. E. Brolley, W. C. Dickinson, and R. L. Henkel, Angular dependence of the neutron-induced fission process. II, Phys. Rev. **99**, 159 (1955).

[41] L. S. Leong, Fission fragment angular distributions and fission cross section validation, Ph.D. thesis, Université Paris Sud, France, 2013 (unpublished).

[42] I. V. Ryzhov *et al.*, Influence of multichance fission on fragment angular anisotropy in the ^{232}Th(n, f) and ^{238}U(n, f) reactions at intermediate energies, Nucl. Phys. A **760**, 19 (2005).

[43] B. M. Gokhberg, L. D. Kozlov, S. K. Lisin *et al.*, Differences between angular distributions of fission fragments of unequal mass, Sov. J. Nucl. Phys. **47**, 201 (1988).

[44] J. Caruana, J. W. Boldeman, and R. L. Walsh, Fission fragment angular distributions for neutron fission of ^{232}Th and their interpretation with a triple-humped fission barrier, Nucl. Phys. A **285**, 205 (1977).

[45] G. Barreau, C. E. N. Bordeaux-Gradignan Rep. **7706** (1977).

[46] S. B. Ermagambetov and G. N. Smirenkin, Fragment angular distributions and channel analysis of fission of 90-Th-232 by neutrons, Sov. J. Nucl. Phys. **11**, 646 (1970).

[47] R. L. Henkel and J. E. Brolley, Jr., Angular distribution of fragments from neutron-induced fission of U-238 and Th-232, Phys. Rev. **103**, 1292 (1956).

[48] D. Tarrío, L. Leong, Audouin *et al.* (n_TOF Collaboration), Fission fragment angular distribution of ^{232}Th(n, f) at the CERN n_TOF facility, Nucl. Data Sheets **119**, 35 (2014).

[49] A. D. Carlson, V. Pronyaev, R. Capote *et al.*, Evaluation of the neutron data standards, Nucl. Data Sheets **148**, 143 (2018); see also http://www-nds.iaea.org/standards/.

[50] Y. Watanabe, K. Kosako, S. Kunieda *et al.*, Status of JENDL high energy file, J. Korean Phys. Soc. **59**, 1040 (2011).

[51] S. Lo Meo, D. Mancusi, C. Massimi, G. Vannini, and A. Ventura, Fission induced by nucleons at intermediate energies, Nucl. Phys. A **933**, 43 (2015).

[52] B. Marcinkevicius, S. Simakov, and V. Pronyaev, ^{209}Bi(n, f) and ^{nat}Pb(n, f) Cross sections as a new reference and extension of the ^{235}U, ^{238}U and ^{239}Pu(n, f) standards up to 1 GeV, Report No. INDC(NDS)-0681 (IAEA, Vienna 2015) (upublished).

[53] I. Duran, A. Ventura, S. Lo Meo, D. Tarrío, L. Tassan-Got, and C. Paradela, On the search for a (n,f) cross-section reference at intermediate energies, EPJ Web Conf. **146**, 02032 (2017).

[54] O. Shcherbakov, A. Donets, A. Evdokimov *et al.*, Neutron-induced fission of ^{233}U, ^{238}U, ^{232}Th, ^{239}Pu, ^{237}Np, ^{nat}Pb and ^{209}Bi relative to ^{235}U in the energy range 1–200 MeV, J. Nucl. Sci. Technol. **39**, 230 (2002).

[55] I. B. Fursov, E. Baranov, M. Klemyshev *et al.*, Measurements of the fission cross-section ratios ^{232}Th$/^{235}$U and ^{234}U$/^{235}$U for 0.13-7.4 MeV neutrons, At. Energy **71**, 827 (1991).

[56] P. W. Lisowski, J. L. Ullman, S. J. Balestrini, A. D. Carlson, O. A. Wasson, and N. W. Hill, Neutron induced fission cross section ratios for ^{232}Th, ^{235,238}U, ^{237}Np and ^{239}Pu from 1 to 400 MeV, in *Proceedings of the Conference on Nuclear Data For Science and Technology, Mito, Japan, 1988* (JAERI, 1988), p. 97.

[57] Y. M. Gledenov, Z. Cui, J. Liu *et al.*, Cross section of the ^{232}Th(n, f) reaction in the MeV neutron energy region, Eur. Phys. J. A **58**, 86 (2022).

[58] V. Michalopoulou, M. Axiotis, S. Chasapoglou *et al.*, Measurement of the ^{232}Th(n, f) cross section with quasi-monoenergetic neutron beams in the energy range 2–18 MeV, Eur. Phys. J. A **57**, 277 (2021).

[59] J. Blons, C. Mazur, D. Paya, M. Ribrag, and H. Weigmann, On the existence of triple-humped fission barriers in ^{231,233}Th, Nucl. Phys. A **414**, 1 (1984).

[60] J. W. Meadows, The fission cross section of Th-230 and Th-232 relative to U-235, Argonne National Laboratory Report. No. 83, 1983 (unpublished).

[61] F. Manabe, K. Kanda, T. Iwasaki, H.Terayama, Y. Karino, M. Baba, and N. Hirakawa, Measurements of neutron induced fission cross section ratios of ^{232}Th, ^{233}U, ^{234}U, ^{236}U, ^{238}U, ^{237}Np, ^{242}Pu and ^{243}Am relative to ^{235}U around 14 MeV, Faculty of Engineering, Tohoku University Technical Report No. 52, 1988 (unpublished), p. 97.

[62] J. W. Meadows, The fission cross sections of ^{230}Th, ^{232}Th, ^{233}U, ^{234}U, ^{236}U, ^{238}U, ^{237}Np, ^{239}Pu and ^{242}Pu relative to ^{235}U at 14.74 MeV neutron energy, Ann. Nucl. Energy **15**, 421 (1988).

[63] F. Belloni, M. Calviani, N. Colonna *et al.* (n_TOF Collaboration), Neutron-induced fission cross-section of ^{233}U in the energy range $0.5 < E_n < 20$ MeV, Eur. Phys. J. A **47**, 2 (2011).

[64] F. Tovesson, A. Laptev, and T. S. Hill, Fast neutron-induced fission cross sections of ^{233,234,236,238}U up to 200 MeV, Nucl. Sci. Eng. **178**, 57 (2014).

[65] K. Guber, R. R. Spencer, L. C. Leal *et al.*, New high-resolution fission cross-section measurements of ^{233}U in the 0.4-eV to 700-keV energy range, Nucl. Sci. Eng. **135**, 141 (2000).

[66] M. Calviani, J. Praena, U. Abbondanno *et al.* (n_TOF Collaboration), High-accuracy ^{233}U(n, f) cross-section measurement at the white-neutron source n_TOF from near-thermal to 1 MeV neutron energy, Phys. Rev. C **80**, 044604 (2009).

[67] G. Noguere and R. Capote, International Nuclear Data Evaluation Network (INDEN) on actinide evaluation in the resonance region (3). Summary report of the consultants' meeting, 17–19 November 2020 (virtual event), Report No. INDC(NDS) 0818, 2021 (unpublished).

[68] A. Blokhin *et al.*, New version of neutron evaluated data library BROND-3.1, Yad. Reak. Konst. **2**, 62 (2016).

[69] Z. Ge, R. Xu, H. Wu *et al.*, CENDL-3.2: The new version of Chinese general purpose evaluated nuclear data library, EPJ Web Conf. **239**, 09001 (2020).

[70] A. Koning, D. Rochman, J. Sublet *et al.*, TENDL: Complete nuclear data library for innovative nuclear science and technology, Nucl. Data Sheets **155**, 1 (2019).

[71] J. Cugnon, C. Volant, and S. Vuillier, Improved intranuclear cascade model for nucleon-nucleus interactions, Nucl. Phys. A **620**, 475 (1997).

[72] A. A. Kotov, L. A. Vaishnene, V. G. Vovchenko *et al.*, Energy dependence of proton induced fission cross sections for heavy nuclei in the energy range 200–1000 MeV, Phys. Rev. C **74**, 034605 (2006).

[73] A. N. Smirnov, V. P. Eismont, I. V. Ryzhov *et al.*, Proton- and neutron-induced fission cross sections and fission probability in the intermediate energy region, J. Nucl. Sci. Technol. **39**, 238 (2002).

[74] A. I. Obukhov, Nuclear fission induced by intermediate-energy protons and neutrons, Phys. Part. Nuclei **32**, 162 (2001).